




Computational and experimental (re)investigation of the structural and electrolyte properties of $\text{Li}_4\text{P}_2\text{S}_6$, $\text{Na}_4\text{P}_2\text{S}_6$, and $\text{Li}_2\text{Na}_2\text{P}_2\text{S}_6$

Yan Li ¹, Zachary D. Hood,² and N. A. W. Holzwarth ¹

¹*Department of Physics, Wake Forest University, Winston-Salem, North Carolina 27109, USA*

²*Department of Materials Science and Engineering, Massachusetts Institute of Technology, Cambridge, Massachusetts 02139, USA*

 (Received 28 January 2020; accepted 24 March 2020; published 21 April 2020)

The ionic materials $\text{Li}_4\text{P}_2\text{S}_6$ and $\text{Na}_4\text{P}_2\text{S}_6$ are both based on the same building blocks of the dimer ions $(\text{P}_2\text{S}_6)^{4-}$. Motivated by new experimental structural and ion conductivity studies, we computationally examine this family of materials, finding $\text{Na}_4\text{P}_2\text{S}_6$ and its modification $\text{Li}_2\text{Na}_2\text{P}_2\text{S}_6$ to be promising Na ion electrolytes. Using first-principles calculations based on density functional theory and density functional perturbation theory within the harmonic phonon approximation, we show that vibrational effects provide nontrivial contributions to the structural stabilization of these materials. Computed nonresonant Raman phonon spectra and temperature-dependent ionic conductivity for $\text{Na}_4\text{P}_2\text{S}_6$ are both found to be in reasonable agreement with experiment. First-principles analysis of ionic conductivity in both $\text{Na}_4\text{P}_2\text{S}_6$ and $\text{Li}_2\text{Na}_2\text{P}_2\text{S}_6$ indicates that Na ions move primarily within the interlayer region between the $(\text{P}_2\text{S}_6)^{4-}$ layers, efficiently proceeding via direct or indirect hops between vacancy sites, with indirect processes involving intermediate interstitial sites.

DOI: [10.1103/PhysRevMaterials.4.045406](https://doi.org/10.1103/PhysRevMaterials.4.045406)

I. INTRODUCTION

There is growing interest in developing all-solid-state batteries for stable and efficient energy storage applications. For example, a recent review [1] notes that inorganic solid electrolytes “lie at the heart of the solid-state battery concept,” stressing the importance of basic research for expanding our knowledge of the fundamental properties of these materials. As particular examples, alkali metal hexathiohypodiphosphate materials $\text{Li}_4\text{P}_2\text{S}_6$ and $\text{Na}_4\text{P}_2\text{S}_6$ and their modifications are of interest to the effort of developing all solid-state batteries. While $\text{Li}_4\text{P}_2\text{S}_6$ has been found to have very small ionic conductivity [2–4], and is cited [5] as a decomposition product in the preparation of lithium thiophosphate electrolytes, $\text{Na}_4\text{P}_2\text{S}_6$ [6] appears to be a competitive electrolyte for sodium ion batteries. Recent experiments [6,7] have provided new structural and electrochemical results which prompt a reexamination of previous computational studies on these materials [2,8] and also prompt an investigation of their modifications, resulting in the prediction of a new promising Na ion electrolyte having the composition $\text{Li}_2\text{Na}_2\text{P}_2\text{S}_6$.

$\text{Li}_4\text{P}_2\text{S}_6$ and $\text{Na}_4\text{P}_2\text{S}_6$ have very similar chemical and structural properties based on the same building blocks of $(\text{P}_2\text{S}_6)^{4-}$ (hexathiohypodiphosphate) complex ions which have D_{3d} point symmetry and typically align along the crystallographic c axis. The crystal structure of $\text{Li}_4\text{P}_2\text{S}_6$ was analyzed by Mercier *et al.* in 1982 [9], finding a disordered lattice with space group $P6_3/mcm$ (No. 193) [10]. Hood *et al.* [2] showed that the disordered Mercier structure could be explained by the energetic insensitivity of the system to the detailed layer arrangements of the $(\text{P}_2\text{S}_6)^{4-}$ complex ions. In that paper, the disordered Mercier structure was categorized in terms of the placements of the $(\text{P}_2\text{S}_6)^{4-}$ ions along the hexagonal c axes using the labels \mathbf{P}_\uparrow and \mathbf{P}_\downarrow . For the few

example structures we investigated, the lowest-energy structures were those with 50% \mathbf{P}_\uparrow and 50% \mathbf{P}_\downarrow , while the structure with 100% \mathbf{P}_\uparrow has the higher-symmetry space group $P\bar{3}1m$ (No. 162) [10], with an energy of 0.03 eV per formula unit higher than the lowest-energy structures. More recently, Neuberger *et al.* [7] showed that it is possible to prepare more highly crystalline samples. These samples, when analyzed with a combination of x-ray analysis and nuclear magnetic resonance (NMR) measurements, were found to have an ordered structure with two inequivalent P sites and to be characterized with the space group $P321$ (No. 150) [10] with three formula units per unit cell. This new analysis provides an explanation of how twinning and poor crystallinity may result in samples consistent with the disordered Mercier structure [9]. The Neuberger analysis supersedes the incorrect analysis of Dietrich *et al.* [3] and approximately corresponds to a Mercier-type structure with $\frac{1}{3} \mathbf{P}_\uparrow$ and $\frac{2}{3} \mathbf{P}_\downarrow$. However, for reasons discussed below, we will reference the Neuberger structure in terms of the $P\bar{3}m1$ space group (No. 164) [10].

Meanwhile, the analogous sodium ion material $\text{Na}_4\text{P}_2\text{S}_6$ was synthesized by Kuhn *et al.* [11] and shown to be characterized by an ordered based-centered monoclinic structure with space group $C2/m$ (No. 12) [10]. Simulations by Rush *et al.* [8] suggested that the $C2/m$ structure may be metastable with respect to lower-energy configurations analogous to the $\text{Li}_4\text{P}_2\text{S}_6$ materials. However, recent experimental results of Hood *et al.* [6] on $\text{Na}_4\text{P}_2\text{S}_6$ find its ground-state structure to be the $C2/m$ structure of Kuhn [11] and also find that it has very promising ionic conductivity.

In view of the new experimental findings, this paper reports a reexamination of our earlier work on $\text{Li}_4\text{P}_2\text{S}_6$ and $\text{Na}_4\text{P}_2\text{S}_6$ and also considers a possible mixed-ion material with the composition $\text{Li}_2\text{Na}_2\text{P}_2\text{S}_6$. Our goal is to determine whether modified and enhanced computational methods can explain

the observed ground-state structures of these materials and to explore mechanisms of Na ion conductivity in $\text{Na}_4\text{P}_2\text{S}_6$ and $\text{Li}_2\text{Na}_2\text{P}_2\text{S}_6$. The remainder of the paper is organized as follows. Section II presents the formalism and computational methods used in this work. Section III presents the computational results for the structural analysis of $\text{Li}_4\text{P}_2\text{S}_6$ and $\text{Na}_4\text{P}_2\text{S}_6$, including the static lattice results in Sec. III A and the effects of phonon energies within the harmonic approximation in Sec. III B. Section III B 1 presents the phonon dispersion curves and comparison between the calculated and measured Raman phonon spectrum for $\text{Na}_4\text{P}_2\text{S}_6$, while Sec. III B 2 presents the phonon dispersion curves for $\text{Li}_4\text{P}_2\text{S}_6$. Results for the phonon contributions to the stabilization of the crystalline phases of both $\text{Na}_4\text{P}_2\text{S}_6$ and $\text{Li}_4\text{P}_2\text{S}_6$ are presented in Sec. III C. Section IV presents results on the most stable structure of $\text{Li}_2\text{Na}_2\text{P}_2\text{S}_6$. Section V examines the Na ion conductivity properties of $\text{Na}_4\text{P}_2\text{S}_6$ and $\text{Li}_2\text{Na}_2\text{P}_2\text{S}_6$. Section VI contains the discussion and conclusions.

II. CALCULATIONAL METHODS

A. General formalism and software implementation

The calculations in this study were based on density functional theory (DFT) [12,13] and density functional perturbation theory (DFPT) [14–18] implemented in the ABINIT [19] and QUANTUM ESPRESSO [20] codes, using the projector augmented plane-wave (PAW) [21] method and using atomic data sets generated with the ATOMPAW code [22]. These data sets were generated with the most recent version of the ATOMPAW code which has been modified for better compatibility with the QUANTUM ESPRESSO formalism [23]. The software packages VESTA [24] and XCRYSDEN [25] were used for visualizations of structural configurations and FINDSYM [26] helped with the space-group analysis of the structures. The MERCURY software package [27] was used to simulate x-ray patterns from calculation results and from published structural data. Additionally, the Bilbao Crystallographic Server [28] was used to help with the symmetry analysis.

Our previous simulation studies of ion conducting materials [2,8] used the exchange-correlation functional of the local density approximation (LDA) [29] because of its generally good representation of vibrational properties of materials [30]. However, in this work, it is necessary to reexamine these previous simulations. Encouraged by recent reports by Petretto *et al.* [31] and by He *et al.* [32] in simulating structural and vibrational spectra for a wide range of inorganic materials in reasonable agreement with experiment, we were motivated to adopt the exchange-correlation functional based on a modified generalized gradient formulation known as PBEsol [33].

B. Formalism for evaluating phase stability

1. First-principles estimation of the Helmholtz free energy

For a system held at constant temperature T and volume V , the equilibrium state is described by a minimum of the Helmholtz free-energy function $F(T, V)$. Within the framework of the Born-Oppenheimer approximation [34] and the harmonic phonon approximation [14,35], $F(T)$ is determined

by a sum of two terms¹

$$F(T) = F_{\text{SL}}(T) + F_{\text{vib}}(T), \quad (1)$$

where the subscript “SL” denotes the static lattice energy at equilibrium and the subscript “vib” denotes the harmonic phonon contribution. For insulating materials in their ground state,

$$F_{\text{SL}}(T) \approx U_{\text{SL}}, \quad (2)$$

the static lattice Helmholtz free energy is approximately temperature independent and determined by the internal energy U_{SL} which is well approximated by the total energy of the system determined from DFT [12,13], optimized with respect to the crystalline lattice vectors and atomic positions. In fact, our previous simulation studies of the materials [2,8] considered only this static lattice contribution. In this work, U_{SL} was evaluated using both ABINIT using a plane-wave cutoff for representing the valence wave functions of $|\mathbf{k} + \mathbf{G}|^2 \leq 50$ Ry and QUANTUM ESPRESSO using a slightly larger plane-wave cutoff of $|\mathbf{k} + \mathbf{G}|^2 \leq 64$ Ry. Here, \mathbf{k} and \mathbf{G} represent an electronic wave vector and reciprocal lattice vector, respectively. For calculations using primitive unit cells, the Brillouin zone sampling of the electronic Bloch wave vector \mathbf{k} used Monkhorst-Pack grids [36] of $3 \times 3 \times 4$ for the $P\bar{3}m1$ structure and $6 \times 6 \times 6$ for the $C2/m$ and $P\bar{3}1m$ structures. For calculations using supercells, the Brillouin zone sampling was adjusted accordingly.

For evaluating the contribution to the Helmholtz free energy due to phonon vibrations in the harmonic phonon approximation [14] we use DFPT which has been implemented in both ABINIT and QUANTUM ESPRESSO. We follow a procedure similar to that described in several references including one by Howard *et al.* [37], as summarized briefly as follows. The harmonic phonon approximation is based on the assumption that it is sufficiently accurate to describe variations of the equilibrium atomic geometry of the static lattice by a Taylor series of small deviations in the atomic displacements of U_{SL} up to quadratic order. This approximation does not include any effects of thermal expansion, and the vibrational frequencies derived from the analysis are independent of temperature. The corresponding vibrational Helmholtz free energy $F_{\text{vib}}(T)$ is explicitly given by the equation

$$F_{\text{vib}}(T) = \int_0^\infty d\omega f_{\text{vib}}(\omega, T), \quad (3)$$

where the weighted phonon density of states factor $f_{\text{vib}}(\omega, T)$ is defined as [35]

$$f_{\text{vib}}(\omega, T) = k_B T \ln \left[2 \sinh \left(\frac{\hbar\omega}{2k_B T} \right) \right] g(\omega). \quad (4)$$

Here, k_B is the Boltzmann constant and $g(\omega)$ denotes the phonon density of states normalized to $3N$ for a material with N atoms in the unit cell. The weighted phonon density of states factor $f_{\text{vib}}(\omega, T)$ is derived from the distribution

¹For notational simplicity, the Helmholtz free energy is written $F(T)$, suppressing the volume dependence in order to focus on the temperature dependence.

of quantum mechanical harmonic oscillator states [35]. In order to assess the contributions of various phonon modes to the vibrational free energy, it is also convenient to define an integrated weighted phonon density of states factor

$$f_{\text{vib}}^{\text{int}}(\omega, T) \equiv \int_0^\omega f_{\text{vib}}(\omega', T) d\omega'. \quad (5)$$

The phonon density of states $g(\omega)$ is determined from a knowledge of the frequencies of the normal modes of vibration $\omega_\nu(\mathbf{q})$ as a function of phonon wave vector \mathbf{q} :

$$g(\omega) = \frac{V}{(2\pi)^3} \int d^3q \sum_{\nu=1}^{3N} \delta(\omega - \omega_\nu(\mathbf{q})), \quad (6)$$

where the integral is taken throughout the unit cell. For our three-dimensional systems, the integral of Eq. (6) is equal to the total number of normal modes of the evaluation cell ($3N$) which is 108, 36, and 36 for the $P\bar{3}m1$, $C2/m$, and $P\bar{3}1m$ structures, respectively.

2. Normal-mode analysis

The normal-mode frequencies $\omega_\nu(\mathbf{q})$ are found by solving eigenvalue problems of the form

$$M_s \omega_\nu^2(\mathbf{q}) u_{si}^v(\mathbf{q}) = \sum_{tj} \tilde{C}_{si,tj}(\mathbf{q}) u_{tj}^v(\mathbf{q}). \quad (7)$$

Here, the indices s, t, \dots denote atoms within the unit cell and the indices i, j, \dots denote Cartesian directions (x, y, z). M_s denotes the atomic mass of the atom at site s . The matrix $\tilde{C}_{si,tj}(\mathbf{q})$ is the Fourier transform of the matrix of second derivatives of the static lattice energy U_{SL} with respect to small displacements of atoms in the unit cell. Explicitly, the analytic part of the second derivative matrix is given by

$$\tilde{C}_{si,tj}(\mathbf{q}) = \sum_m \frac{\partial^2 U_{\text{SL}}(\{\mathbf{u}\})}{\partial u_{si}(\mathbf{R}_l) \partial u_{tj}(\mathbf{R}_m)} e^{-i\mathbf{q} \cdot (\mathbf{R}_l - \mathbf{R}_m)}, \quad (8)$$

where \mathbf{R}_l and \mathbf{R}_m represent the positions of the l th and the m th unit cells in the crystal, respectively. Because of the translational symmetry of the lattice, the summation over \mathbf{R}_m in Eq. (8) spans all translation vectors of the unit cell and the result does not depend upon \mathbf{R}_l . The parameters $u_{si}(\mathbf{R}_l)$ represent the displacement in the i direction of atom s from its equilibrium position ($\boldsymbol{\tau}_s + \mathbf{R}_l$) in cell l . For a normal-mode analysis of the system characterized by phonon wave vector \mathbf{q} , $u_{si}(\mathbf{R}_l)$ is related to the normal-mode amplitude $u_{si}^v(\mathbf{q})$ according to

$$u_{si}(\mathbf{R}_l) = u_{si}^v(\mathbf{q}) e^{i\mathbf{q} \cdot \mathbf{R}_l}. \quad (9)$$

Within the framework of DFPT, Eq. (8) can be evaluated as in terms of the displacement amplitudes $u_{si}(\mathbf{q})$ according to

$$\tilde{C}_{si,tj}(\mathbf{q}) = \frac{\partial^2 U_{\text{SL}}}{\partial u_{si}^*(\mathbf{q}) \partial u_{tj}(\mathbf{q})}. \quad (10)$$

For ionic materials in the $\mathbf{q} \rightarrow 0$ limit, in addition to the analytic contribution to the dynamical matrix (10), effects due to the coupling of ion motions to long-wavelength electromag-

netic fields [14–18,34,38] must be taken into account. These long-wavelength electromagnetic field couplings lead to the frequency splitting of transverse optical (TO) and longitudinal optical (LO) modes at $\mathbf{q} = 0$ and for hexagonal and other layered geometries as considered in this work, they lead to apparent discontinuities in the phonon dispersion curves $\omega_\nu(\mathbf{q})$ for some of the normal modes [38].

It is convenient to define an atomic weight factor which represents the contribution of each atom type a among the sites s to the mode ν according to

$$W_a^v(\mathbf{q}) \equiv \sum_{s \in a, i} |e_{si}^v(\mathbf{q})|^2, \quad (11)$$

where the normalized eigenvectors are defined according to

$$e_{si}^v(\mathbf{q}) = \sqrt{M_s} u_{si}^v(\mathbf{q}) \quad \text{where} \quad \sum_{si} |e_{si}^v(\mathbf{q})|^2 = 1. \quad (12)$$

Using atomic weight factors given by Eq. (11) for each normal mode, a projected density of phonon modes function (PJDOS) for each atomic type can then be defined according to

$$g^a(\omega) \equiv \frac{V}{(2\pi)^3} \int d^3q \sum_{\nu=1}^{3N} (\delta(\omega - \omega_\nu(\mathbf{q})) W_a^v(\mathbf{q})). \quad (13)$$

Defined in this way, it is apparent that

$$\sum_a g^a(\omega) = g(\omega). \quad (14)$$

In practice, it is of interest to examine the dispersion of the normal-mode frequencies $\omega_\nu(\mathbf{q})$ plotted along various lines within the Brillouin zone. In order to facilitate analysis of the phonon dispersion curves $\omega_\nu(\mathbf{q})$ and projected densities of states $g^a(\omega)$ functions, both ABINIT and QUANTUM ESPRESSO use interpolations based on Eq. (8) evaluated from the DFPT results of the unique \mathbf{q} points on a coarser Brillouin zone sampling grid. In this work the coarse Brillouin zone sampling grids for the phonon wave vectors \mathbf{q} were based on Monkhorst-Pack grids [36] using $3 \times 3 \times 4$ for the $P\bar{3}m1$ structure and $3 \times 3 \times 3$ for the $C2/m$ and $P\bar{3}1m$ structures. All of these quantities provide insight into the factors which contribute to minimizing the Helmholtz free energy [Eq. (1)] which thus determine the most stable phase at any given temperature.

3. Analysis of nonresonant Raman spectra

For purposes of validation, it is helpful to compare computed and measured results whenever possible. In this case, nonresonant Raman spectra have been measured for samples of $\text{Na}_4\text{P}_2\text{S}_6$ [6]. Furthermore, with an updated version of ABINIT [39], it is now possible to make a first-principles estimate of Raman spectra within the PAW formalism [21], although restricted only to the local density approximation (LDA) [29] exchange-correlation functionals. Accordingly, for this portion of the calculation only, we used atomic data sets generated by ATOMPAW [22] with the LDA exchange-correlation functionals. Past experience [40] shows that this functional generally gives excellent results for phonon frequencies while systematically underestimating lattice equilibrium lattice constants in terms of agreement with experimental measurements.

There have been a number of papers in the literature detailing the equations for first-principles estimations of Raman spectra. In this work we follow the work and approximate the notation of Umari *et al.* [41], Veithen *et al.* [42], and Prosandeev *et al.* [43]. We assume that the sample is composed of randomly oriented crystals and that the measured spectrum is unpolarized. For the Stokes shifted spectrum with an assumed Lorentzian line shape, the Raman intensity $I(\omega)$ as a function of frequency ω can be expressed according to

$$I(\omega) = \sum_{\nu} \left\langle \frac{d\sigma}{d\Omega} \right\rangle^{\nu} \frac{\Gamma^{\nu}}{(\omega - \omega_{\nu})^2 + \Gamma^{\nu 2}}. \quad (15)$$

Here, the sum over ν includes all of the Raman active normal modes with frequencies ω_{ν} . Γ^{ν} represents a linewidth parameter that is estimated empirically. The orientationally averaged Raman power cross section is given by [41]

$$\left\langle \frac{d\sigma}{d\Omega} \right\rangle^{\nu} = \mathcal{V} \frac{\hbar(\omega_I - \omega_{\nu})^4 [n_{\nu}(T) + 1]}{2\omega_{\nu}c^4} |\langle \alpha_{ij}^{\nu} \rangle|^2. \quad (16)$$

Here, \mathcal{V} represents the volume of the scattering sample, c is the speed of light, ω_I denotes the frequency of the incident laser light, and $n_{\nu}(T)$ represents the temperature-dependent Bose-Einstein distribution of the mode ν :

$$n_{\nu}(T) = \frac{1}{e^{\hbar\omega_{\nu}/k_B T} - 1}. \quad (17)$$

The Raman matrix element for scattered light direction i and incident light direction j for mode ν is given in terms of the the displacement derivative of the electronic dielectric matrix ϵ_{ij}^{∞} according to

$$\alpha_{ij}^{\nu} = \frac{\sqrt{V}}{4\pi} \sum_{sk} \frac{\partial \epsilon_{ij}^{\infty}}{\partial \tau_{sk}} u_{sk}^{\nu}. \quad (18)$$

Here, the summation goes over all atoms s in the unit cell and all Cartesian directions k . τ_{sk} denotes the k th component of the equilibrium position of atom s within a unit cell and u_{sk}^{ν} denotes the k th component of atom s of phonon eigenvector of Eq. (7) evaluated for $\mathbf{q} = 0$. The orientational averaging can be expressed in terms of invariants of $|\langle \alpha_{ij}^{\nu} \rangle|^2$ according to [43,44]

$$|\langle \alpha_{ij}^{\nu} \rangle|^2 = \frac{1}{30} (10G_{\nu}^{(0)} + 5G_{\nu}^{(1)} + 7G_{\nu}^{(2)}), \quad (19)$$

where

$$\begin{aligned} G_{\nu}^{(0)} &= \frac{1}{3} (\alpha_{xx}^{\nu} + \alpha_{yy}^{\nu} + \alpha_{zz}^{\nu})^2 \\ G_{\nu}^{(1)} &= \frac{1}{2} ((\alpha_{xy}^{\nu} - \alpha_{yx}^{\nu})^2 + (\alpha_{xz}^{\nu} - \alpha_{zx}^{\nu})^2 + (\alpha_{yz}^{\nu} - \alpha_{zy}^{\nu})^2) \\ G_{\nu}^{(2)} &= \frac{1}{2} ((\alpha_{xy}^{\nu} + \alpha_{yx}^{\nu})^2 + (\alpha_{xz}^{\nu} + \alpha_{zx}^{\nu})^2 + (\alpha_{yz}^{\nu} + \alpha_{zy}^{\nu})^2) \\ &\quad + \frac{1}{3} ((\alpha_{xx}^{\nu} - \alpha_{yy}^{\nu})^2 + (\alpha_{xx}^{\nu} - \alpha_{zz}^{\nu})^2 + (\alpha_{yy}^{\nu} - \alpha_{zz}^{\nu})^2). \end{aligned} \quad (20)$$

C. Formalism for modeling ionic conductivity

1. Nudged elastic band (NEB) calculations

As in previous work [2,8], the ‘‘nudged elastic band’’ (NEB) approach [45–47] was used to estimate the Na ion migration energy E_m . For both $\text{Na}_4\text{P}_2\text{S}_6$ and $\text{Li}_2\text{Na}_2\text{P}_2\text{S}_6$ in the $C2/m$ structure, simulations were performed on supercells constructed from primitive cells multiplied by $2 \times 1 \times 2$. In addition to simulating the energy path diagram for Na ion vacancies between adjacent host lattice sites in order to estimate E_m , this same supercell was used to estimate the formation energy E_f as the static lattice energy difference from the perfect supercell and one with a host lattice Na ion placed in an interstitial position, forming a vacancy-interstitial pair. From these results we can infer that the activation energy E_a for Na ion conductivity can be estimated as

$$E_m \leq E_a^{\text{NEB}} \leq E_m + \frac{1}{2} E_f. \quad (21)$$

Here, the upper estimate represents the case for a well-formed sample with few native vacancies, while the lower estimate represents the case for a sample with a significant population of vacancies. It is generally expected that the temperature (T) dependence of the conductivity is described by an Arrhenius relationship

$$\sigma(T) = \frac{A}{T} e^{-E_a^{\text{NEB}}/k_B T}, \quad (22)$$

where A is a temperature-independent constant and k_B denotes the Boltzmann constant.

2. Molecular dynamics simulations

First-principles molecular dynamics simulations were performed by using QUANTUM ESPRESSO [20], focusing on the investigation of Na ion diffusion in both $\text{Na}_4\text{P}_2\text{S}_6$ and $\text{Li}_2\text{Na}_2\text{P}_2\text{S}_6$. For each material, the simulations were carried out for a supercell constructed with $2 \times 1 \times 2$ conventional unit cells and eight formula units, using a minimal zero-center \mathbf{k} -point sampling grid $1 \times 1 \times 1$. The plane-wave expansion included $|\mathbf{k} + \mathbf{G}| \leq 64$ Ry and the energy tolerance of the self-consistent field was set to 10^{-8} Ry. Each simulation used a time step of $\Delta t = 2.4$ fs in a microcanonical ensemble (NVE) and the Verlet algorithm [48] was chosen to integrate the equation of motion. Since the equations of motion conserve the simulation energy E , the average temperature can be determined for each ensemble from the average kinetic energy of the simulation. Due to the temperature fluctuations within each simulation, the temperature cannot be precisely set by this procedure, but the approximate temperature can be controlled by setting the initial conditions of each simulation. This approach and choice of parameters gave good results in previous molecular dynamics studies of ionic conductors by our group [37]. Compared to the NEB approach for studying ion hops along a presumed migration pathway, the molecular dynamics simulations model the dynamics of motions of the ensemble of ions within the femtosecond timescale. Thus, it is possible to display more diffusion pathways and reveal new diffusion mechanisms.

In order to quantify the molecular dynamics results in terms of Na ion conductivity, we use the approximate treatment based on the mean-squared displacements (MSD)

of the mobile Na ions. Denoting by $\mathbf{r}_s(t)$ the trajectory of the s th ion as a function of time t , the MSD is given by

$$\text{MSD}(t, T) \equiv \frac{1}{N_{\text{Na}}} \left\langle \sum_{s=1}^{N_{\text{Na}}} |\mathbf{r}_s(t) - \mathbf{r}_s(0)|^2 \right\rangle_T. \quad (23)$$

Here, N_{Na} represents the number of Na ions in the simulation cell. The angular brackets represent an ensemble average which in practice is achieved by averaging the expression over multiple trajectories with the same time interval t [49]. The subscript T denotes the average temperature of the simulation. In the limit of long simulation times, the MSD is related to the tracer diffusion $D_{\text{tr}}(T)$ which in turn has an Arrhenius dependence on the simulation temperature T . For a three-dimensional system,

$$D_{\text{tr}}(T) = \frac{1}{6} \lim_{t \rightarrow \infty} \left(\frac{\text{MSD}(t, T)}{t} \right) = D_0 e^{-E_a^{\text{MSD}}/k_B T}. \quad (24)$$

For this system, the Nernst-Einstein relationship between the electrical conductivity and the tracer diffusion coefficient [50,51] is given by

$$\sigma(T) = \frac{N_{\text{Na}} e^2 D_{\text{tr}}(T)}{V k_B T H_r}. \quad (25)$$

Here, V represent the volume of the simulation cell and H_r denotes the Haven ratio [52,53] which provides a measure of the correlation in the motions of the conducting ions. Comparing the constant coefficients in Eqs. (24) and (22) and assuming that the two activation energies are comparable, we find the Arrhenius constants have the relationship

$$A = \frac{N_{\text{Na}} e^2 D_0}{V k_B H_r}. \quad (26)$$

Here, we see that the molecular dynamics analysis does provide an estimate of the magnitude of ionic conductivity up to the unknown Haven ratio H_r , while the NEB approach does not. In general, the activation energy E_a^{MSD} estimates the ensemble average of single ion processes, while E_a^{NEB} estimates the activation energy for hopping between idealized local minima in Na ion vacancy potential energy surface.

III. ANALYSIS OF STABLE CRYSTAL STRUCTURES OF $\text{Li}_4\text{P}_2\text{S}_6$ and $\text{Na}_4\text{P}_2\text{S}_6$

A. Computed optimized static lattice structures

Based on previous computational experience and new experimental analysis outlined in the Introduction (Sec. I), we focus on three different structures for analyzing the structural properties of $\text{Li}_4\text{P}_2\text{S}_6$ and $\text{Na}_4\text{P}_2\text{S}_6$. These are the trigonal Neuberger structure [7] analyzed for well-crystallized samples of $\text{Li}_4\text{P}_2\text{S}_6$ having three formula units per unit cell, the base-centered monoclinic Kuhn structure [11] analyzed for crystals of $\text{Na}_4\text{P}_2\text{S}_6$ having one formula unit per primitive cell, and the trigonal reference structure having space group $P\bar{3}1m$ which is based on a subgroup of the Mercier structure of $\text{Li}_4\text{P}_2\text{S}_6$ [9] having one formula unit per primitive unit cell. While the $P\bar{3}1m$ structure has not been observed for these materials, it does present a useful reference related to the $C2/m$ structure.

TABLE I. Summary of static lattice results. Lattice constants for the primitive unit cells are listed in units of Å and angles in degrees. The static lattice energy differences ΔU_{SL} are listed as eV/(formula unit) referenced to the energy of the $P\bar{3}1m$ structure.

$\text{Li}_4\text{P}_2\text{S}_6$	a	b	c	α	β	γ	ΔU_{SL}
$P\bar{3}1m^a$	10.42	10.42	6.54	90.0	90.0	120.0	0.00
$C2/m^b$	6.08	6.08	6.89	97.9	97.9	119.1	0.31
$P\bar{3}1m$	6.03	6.03	6.48	90.0	90.0	120.0	0.04
$\text{Na}_4\text{P}_2\text{S}_6$	a	b	c	α	β	γ	ΔU_{SL}
$P\bar{3}1m$	11.10	11.10	7.25	90.0	90.0	120.0	0.00
$C2/m^c$	6.51	6.51	7.52	98.5	98.5	117.6	0.00
$P\bar{3}1m$	6.45	6.45	7.13	90.0	90.0	120.0	0.09

^aCorresponding experimental values quoted from Ref. [7] are $a = b = 10.51$ Å, $c = 6.59$ Å, assuming the closely related space group $P321$.

^bLattice parameters for conventional unit cell are $a_c = 6.17$ Å, $b_c = 10.48$ Å, $c_c = 6.89$ Å, and $\beta_c = 105.8^\circ$.

^cLattice parameters for conventional unit cell are $a_c = 6.74$ Å, $b_c = 11.13$ Å, $c_c = 7.52$ Å, and $\beta_c = 106.5^\circ$. The corresponding experimental values quoted from Ref. [11] are $a_c = 6.725$ Å, $b_c = 11.222$ Å, $c_c = 7.542$ Å, and $\beta_c = 107.03^\circ$.

Table I summarizes the lattice constants and angles computed for these structures. From this table, it is apparent that the calculated structural parameters are very close to the available experimental values, differing by at most 0.1 Å and 1° for the lattice constants and angles. Figures 1(a)–1(c) show the ball and stick models of the three structures. The unique fractional coordinates are given in the Appendix.

In the course of optimizing the Neuberger structure using the experimentally analyzed [7] fractional coordinates for $\text{Li}_4\text{P}_2\text{S}_6$ as a guide, we find that the optimized structure has an additional inversion center compared with $P321$ space group, resulting in the space group $P\bar{3}1m$ (No. 164) [10]. This slightly contradicts the results of Neuberger *et al.* [7], presented in their Supplemental Materials. On the other hand, the x-ray diffraction patterns of the $P\bar{3}1m$ and $P321$ structures, which are shown in Fig. 2, appear to be very similar. In this paper we will refer to the Neuberger structure in terms of the $P\bar{3}1m$ space group.

For the centered monoclinic unit cell $C2/m$ structure of $\text{Na}_4\text{P}_2\text{S}_6$ analyzed by Kuhn *et al.* [11], it is convenient to use the primitive cell vectors (\mathbf{a} , \mathbf{b} , \mathbf{c}) which can be related to the conventional monoclinic cell parameters (a_c , b_c , c_c , β_c) according to [54,55]

$$\begin{aligned} \mathbf{a} &= \frac{1}{2}a_c\hat{\mathbf{x}} - \frac{1}{2}b_c\hat{\mathbf{y}}, \\ \mathbf{b} &= \frac{1}{2}a_c\hat{\mathbf{x}} + \frac{1}{2}b_c\hat{\mathbf{y}}, \\ \mathbf{c} &= c_c \cos \beta_c \hat{\mathbf{x}} + c_c \sin \beta_c \hat{\mathbf{z}}. \end{aligned} \quad (27)$$

Analyzed in terms of the primitive cell parameters, it is apparent from Table I and Figs. 1(b) and 1(c) that the primitive cell form of Kuhn structure is very similar to the simple hexagonal $P\bar{3}1m$ structure.

Also listed in Table I are the static lattice energies ΔU_{SL} referenced to the energy of the $P\bar{3}1m$ structure.

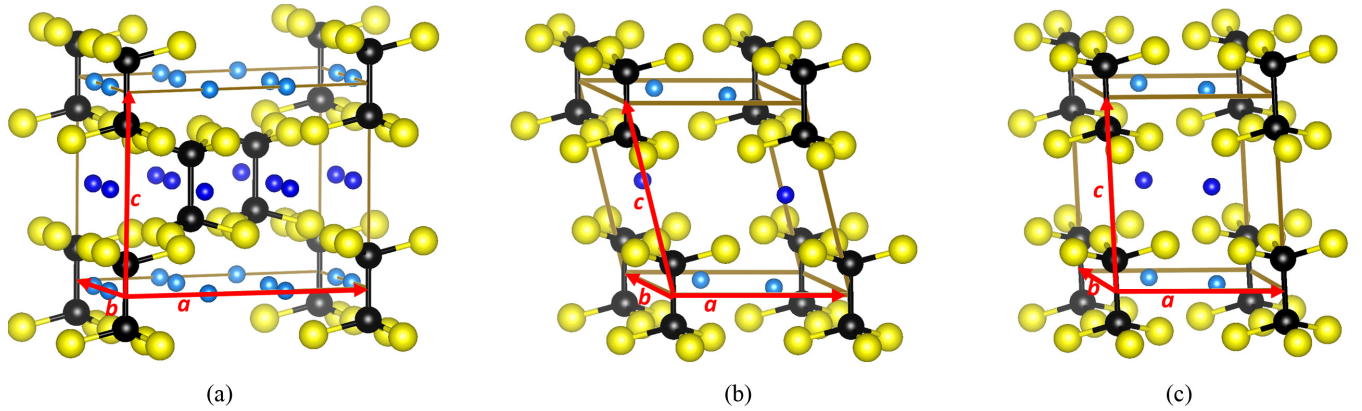


FIG. 1. Ball and stick visualizations of $\text{Li}/\text{Na}_4\text{P}_2\text{S}_6$ in the (a) $P\bar{3}m1$, (b) $C2/m$, and (c) $P\bar{3}1m$ structures showing axes of primitive cell (brown lines and red arrows) with Li/Na, P, and S represented by blue, black, and yellow balls, respectively. Two shades of blue are used to indicate the two inequivalent Li/Na sites in each structure.

The results for the materials in the $C2/m$ and $P\bar{3}1m$ structures are somewhat different from the earlier results by Rush [8] obtained using the LDA exchange-correlation functional. The current results using the PBEsol exchange-correlation functional find the lowest static lattice energy of $\text{Li}_4\text{P}_2\text{S}_6$ in the $P\bar{3}m1$ structure which is consistent with the LDA results which found the related Mercier structures to have the lowest static lattice energies. For $\text{Na}_4\text{P}_2\text{S}_6$, the PBEsol exchange-correlation functional finds the lowest static lattice energies for both the $P\bar{3}m1$ and $C2/m$ structures, while the LDA results found the stability pattern for $\text{Na}_4\text{P}_2\text{S}_6$ to be similar to that of $\text{Li}_4\text{P}_2\text{S}_6$.

B. Phonon contributions

I. $\text{Na}_4\text{P}_2\text{S}_6$

In order to further analyze the structures, we computed the phonon normal modes as explained in Sec. II B using

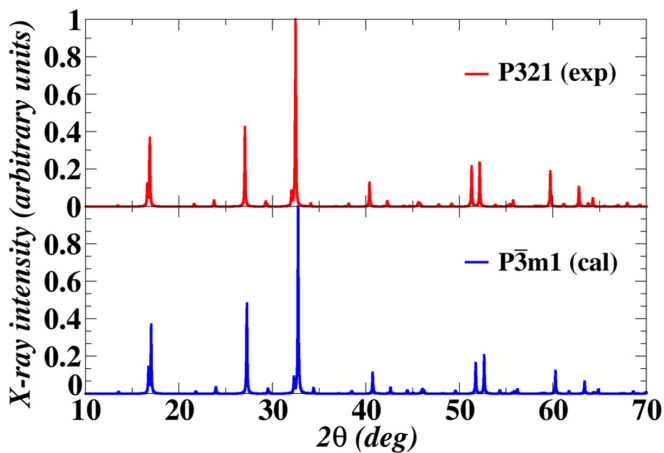


FIG. 2. Comparison of x-ray diffraction patterns for wavelength $\lambda = 1.54 \text{ \AA}$ for $\text{Li}_4\text{P}_2\text{S}_6$ generated from the MERCURY software package [27]. The upper (red) curve represents the experimental analysis [7] analyzed with the $P321$ space group; the lower (blue) curve represents the simulation results having the $P\bar{3}m1$ space group.

DFPT in both the ABINIT and QUANTUM ESPRESSO codes. While the equations in Secs. IIB1–IIB3 reference the phonon frequencies in units of rad/s, the results presented here are instead quoted as $\omega/(2\pi c)$ in units of cm^{-1} (where c denotes the speed-of-light constant). Figure 3 shows the phonon dispersion curves along with the corresponding atom type projected density of states [$g^a(\omega)$] for $\text{Na}_4\text{P}_2\text{S}_6$, comparing results in three considered structures. For each structure, the associated path of high-symmetry \mathbf{q} points is selected as recommended for the type of Bravais lattice with diagrams shown in Figs. 3(d) and 3(e), reproduced from Ref. [56]. In view of the fact that the phonon frequencies throughout the Brillouin zone are real, each structure is predicted to be dynamically stable. The figure shows considerable similarity between the phonon dispersions $\omega_v(\mathbf{q})$ and atom type projected density of states $g^a(\omega)$, for the three structures. While vibrational amplitudes on the S sites occur throughout the frequency range, the Na amplitudes contribute to mode frequencies in the range of 0–300 cm^{-1} . Vibrations in the range 300–600 cm^{-1} generally correspond to modes associated with the $(\text{P}_2\text{S}_6)^{4-}$ dimer ions. In particular, all three structures have two modes per formula unit which are independent of \mathbf{q} , indicating pure internal dimer vibrations. For example, for the $C2/m$ structure, these internal vibrational modes occur near the frequencies $\omega^{30}(\mathbf{q}) = 370 \text{ cm}^{-1}$ and $\omega^{32}(\mathbf{q}) = 540 \text{ cm}^{-1}$ and occur at similar frequencies for the other two structures. For the $P\bar{3}m1$ structure having three formula units per primitive cell, these internal dimer vibrations occur in two groups of three modes each, with a small splitting within each group due to a slight inequivalence of one-third of the $(\text{P}_2\text{S}_6)^{4-}$ placements. The three phonon band plots in Figs. 3(a)–3(c) display the apparent dispersion discontinuities at the Γ point mentioned in Sec. IIB2 [38].

Since the Raman spectrum of $\text{Na}_4\text{P}_2\text{S}_6$ in the $C2/m$ structure has been measured [6], it is useful to examine its Raman active phonon vibrational modes theoretically and computationally. According to group theory analysis [28] of the $\mathbf{q} = 0$ normal modes for this system which is characterized by the C_{2h} point group, the 36 vibrational modes are distributed among the 4 distinct representations according

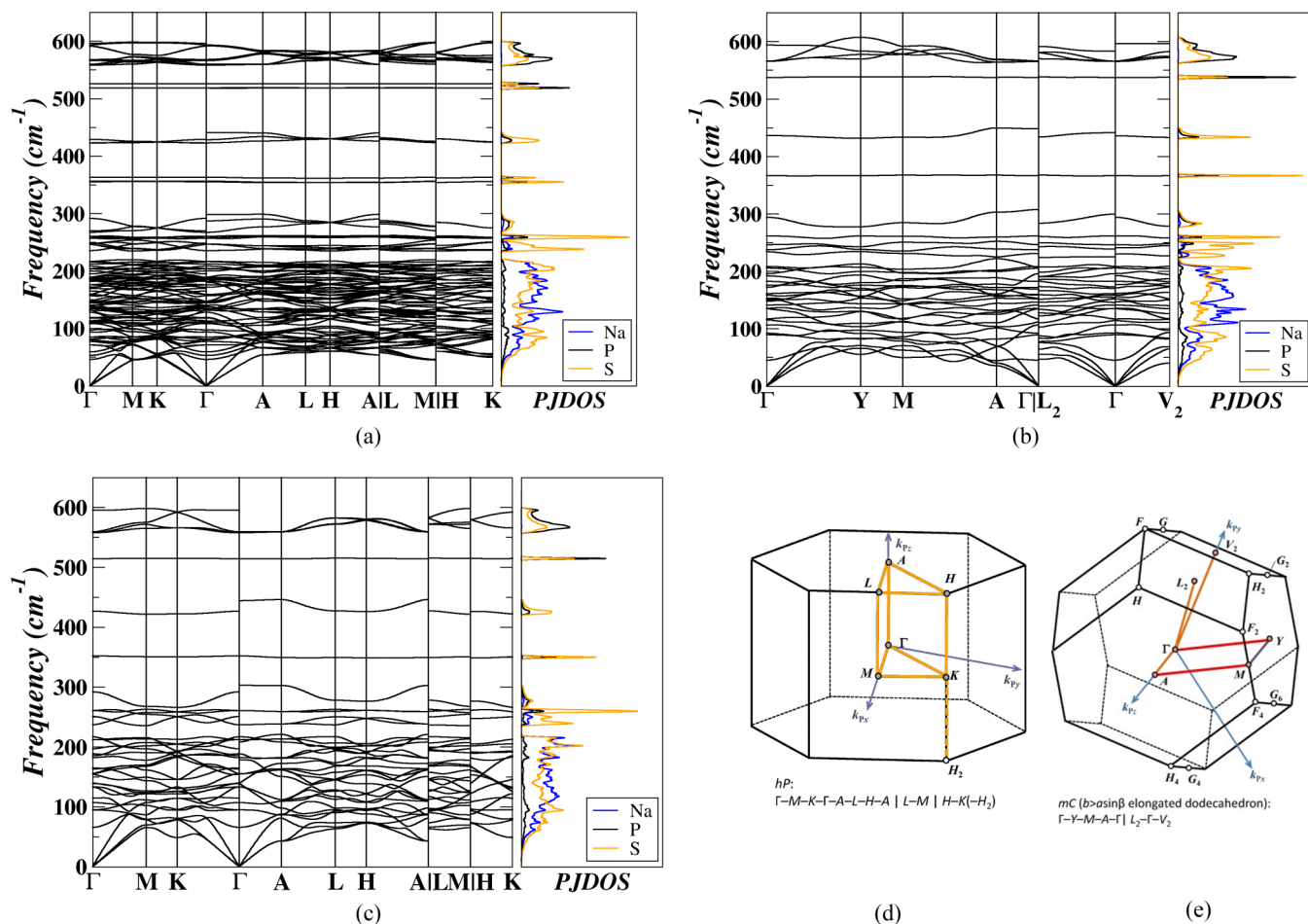


FIG. 3. For $\text{Na}_4\text{P}_2\text{S}_6$, plots of phonon normal-mode frequencies $\omega(\mathbf{q})$ in units of cm^{-1} for (a) $P\bar{3}m1$, (b) $C2/m$, and (c) $P\bar{3}1m$ structures all in their primitive unit cells plotted along various lines within the Brillouin zone. The atom type projected density of states [$g^a(\omega)$, PJDOS] are plotted using the same frequency scale along the right panel of each dispersion plot. Brillouin zone diagrams (d) for the trigonal $P\bar{3}m1$ and $P\bar{3}1m$ structures and diagram (e) for the monoclinic $C2/m$ structure are reproduced from Hinuma *et al.* in Ref. [56] with permission from the publisher.

to $9A_g + 7A_u + 9B_g + 11B_u$. Here, the infrared active modes have symmetry $7A_u + 11B_u$ and the remaining symmetries $9A_g + 9B_g$ are Raman active.

As mentioned in Sec. IIB3, the ABINIT code [39] has not yet implemented the Raman intensity analysis for the PBEsol [33] exchange-correlation functional, but only for the LDA [29] functional. Consequently, it is important to assess how sensitive are the computed phonon frequencies to the choice of exchange-correlation functional. For this test, we used PAW data sets generated with the ATOMPAW [22] code and, as a further check, also use optimized norm-conserving (ONC) developed by Haman [57] which are available from the PSEUDODOJO project [58]. In Fig. 4 we compare the spectra of Raman active mode frequencies computed using the LDA and PBEsol exchange-correlation functionals using both the PAW and ONC data sets. The results show that the phonon frequencies generated with the LDA exchange-correlation functional using the ONC and PAW data sets are essentially identical, while those generated with the PBEsol exchange-correlation functional and the PAW data sets, used in the majority of this paper, are usually shifted to lower frequencies in the range of 5–15 cm^{-1} .

Using DFPT to estimate the Raman spectra of $\text{Na}_4\text{P}_2\text{S}_6$ in the $C2/m$ structure as described in Sec. IIB3 we can make a quantitative comparison with the measured spectrum which

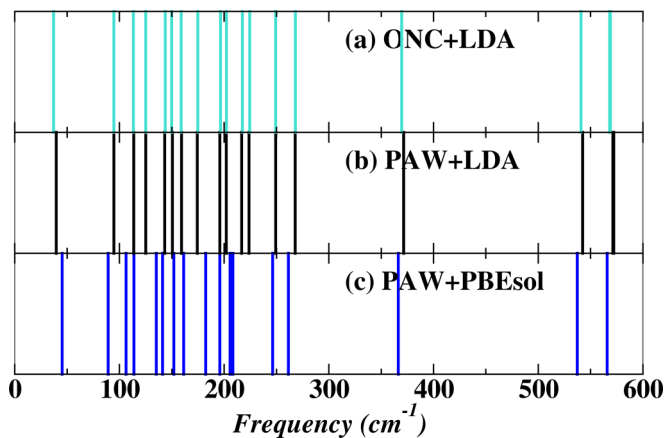


FIG. 4. Frequencies of $\mathbf{q} = 0$ Raman active modes of $\text{Na}_4\text{P}_2\text{S}_6$ in the $C2/m$ structure. Comparing results of (a) ONC, (b) PAW, both using LDA, to the results of (c) PAW using PBEsol.

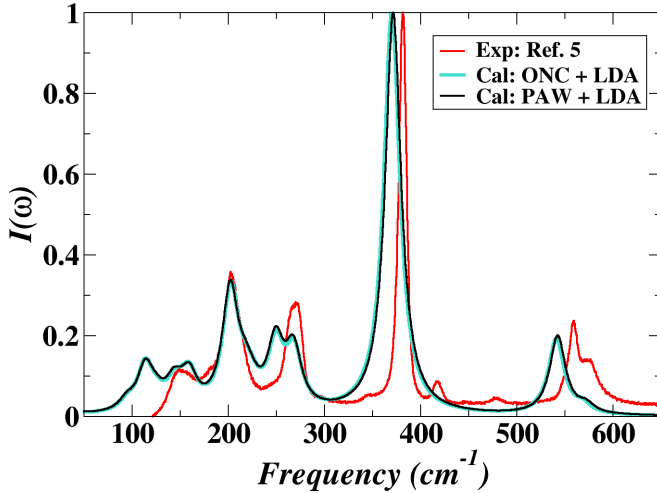


FIG. 5. Calculated Raman intensities for the $C2/m$ structure of $\text{Na}_4\text{P}_2\text{S}_6$ using ONC (turquoise) and PAW (black), in comparison to the experimental spectrum (red) [6] resulting from an incident light wavelength of 532 nm. The calculated spectra used the LDA exchange-correlation functional and were evaluated at $T = 300$ K. For each mode, the Lorentzian linewidth Γ^ν was chosen to be 10 cm^{-1} .

is presented in Fig. 5. For this simulation, we used the LDA exchange-correlation functional and both ONC and PAW data sets. The computed spectra assumed that $T = 300$ K and assumed a constant Lorentzian linewidth of $\Gamma^\nu = 10 \text{ cm}^{-1}$. The computed and experimental intensities were adjusted so that their peak intensities were each scaled to a value of 1. The computed intensity curves using the ONC and PAW are essentially superposed one on another validating both the code implementations of the two formalisms and also validating these ONC and PAW data sets. The results also show a close agreement between the computed and experimental values. For example, both the experiment and calculation observe the highest intensity peak at about 383 and 371 cm^{-1} , respectively. More specifically, this peak corresponds to a normal mode of A_g symmetry associated with the internal stretching motions of the $(\text{P}_2\text{S}_6)^{4-}$ ions. This mode also corresponds to the lowest frequency nondispersive mode mentioned in Sec. III B 1 and shown in Fig. 3(b). In future work, it may be appropriate to further investigate the sensitivity of the computed spectra on the Lorentzian linewidth parameter Γ^ν .

2. $\text{Li}_4\text{P}_2\text{S}_6$

Since the Neuberger [7] preparation of $\text{Li}_4\text{P}_2\text{S}_6$, corresponds to the $P\bar{3}m1$ structure, it is useful to compare its vibrational spectrum with that of $\text{Na}_4\text{P}_2\text{S}_6$ shown in Fig. 3(a) in order to get a sense of the difference caused by replacing Na by Li within the lattice of the same symmetry as shown in Fig. 6. The comparison shows that the vibrational spectra for the two materials are very similar; the main differences are that the Li amplitude motions extend to higher frequencies, 370 cm^{-1} , compared with the corresponding Na amplitude motions.

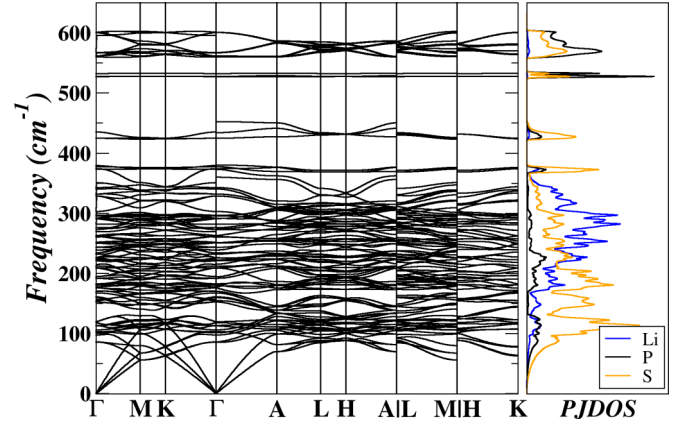


FIG. 6. Phonon band structure and the corresponding projected density of states for $\text{Li}_4\text{P}_2\text{S}_6$ in the $P\bar{3}m1$ structure. See Fig. 3(d) for the Brillouin zone diagram of the hexagonal structure.

C. Helmholtz free energy and stability of crystalline phases

The total Helmholtz free energy of $\text{Na}_4\text{P}_2\text{S}_6$ in each of the three model structures, as evaluated from Eqs. (1)–(3), are shown Fig. 7(a) in comparison with those of $\text{Li}_4\text{P}_2\text{S}_6$ analogs as plotted in Fig. 7(b). The corresponding vibrational free energies F_{vib} near the room temperature are inserted in each subfigure for comparing the contributions to the stability of the crystal. As implied by the overlapped black and purple curves in the inserted figures, the phonon contributions from the two hexagonal structures $P\bar{3}m1$ and $P\bar{3}1m$ are almost identical with energy value higher than that of $C2/m$ structure throughout the temperature range for both materials. In the case of $\text{Na}_4\text{P}_2\text{S}_6$, the lowest Helmholtz free energy of the $C2/m$ structure indicates that the vibrational free energy contributes to the stabilization of this phase. While for $\text{Li}_4\text{P}_2\text{S}_6$, although the $C2/m$ structure possesses the lowest vibrational free energy, it is the static energy U_{SL} that plays a dominant role in stabilizing in the $P\bar{3}m1$ structure.

We present the summary of simulation energies at $T = 300$ K in Table II to detail the relationships between the competing energies. It is interesting to note that at this temperature, $F_{\text{vib}} < 0$ for all of the $\text{Na}_4\text{P}_2\text{S}_6$ structures while $F_{\text{vib}} > 0$ for all of the $\text{Li}_4\text{P}_2\text{S}_6$ structures. It is also interesting to note that the vibrational contributions to the stabilization

TABLE II. Summary of simulation energies for $\text{Na}_4\text{P}_2\text{S}_6$ and $\text{Li}_4\text{P}_2\text{S}_6$ at $T = 300$ K. Results given in units of eV/(formula unit); for each material, the energy zero is set at the static lattice energy U_{SL} for the $P\bar{3}m1$ structure.

$\text{Na}_4\text{P}_2\text{S}_6$	ΔU_{SL}	$F_{\text{vib}} (300 \text{ K})$	$F (300 \text{ K})$
$P\bar{3}m1$	0.00	-0.04	-0.04
$C2/m$	0.00	-0.08	-0.08
$P\bar{3}1m$	0.09	-0.04	0.05
$\text{Li}_4\text{P}_2\text{S}_6$	ΔU_{SL}	$F_{\text{vib}} (300 \text{ K})$	$F (300 \text{ K})$
$P\bar{3}m1$	0.00	0.19	0.19
$C2/m$	0.31	0.12	0.43
$P\bar{3}1m$	0.04	0.20	0.24

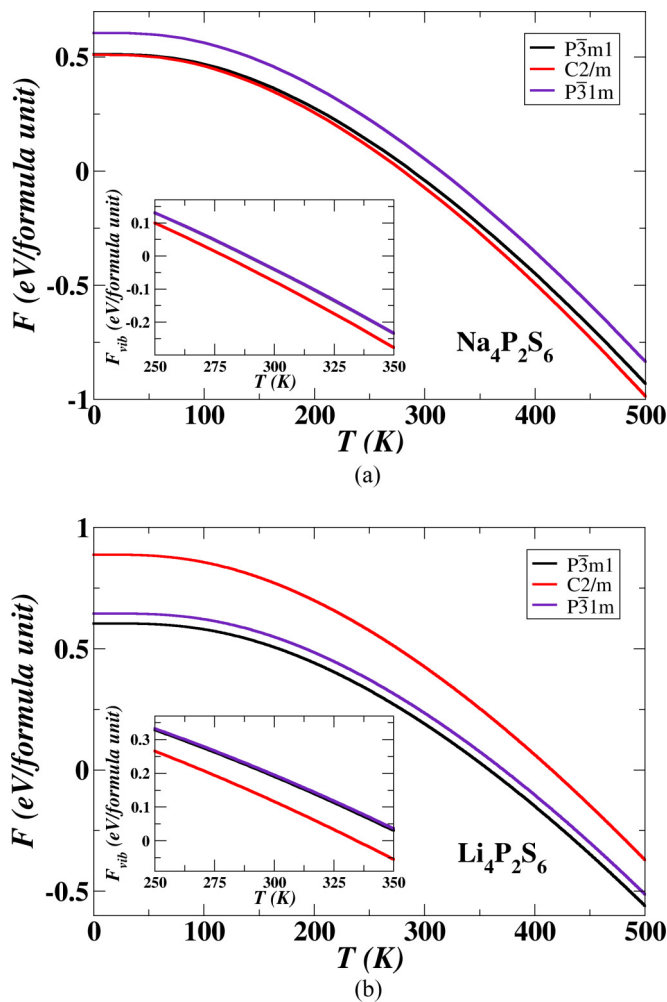


FIG. 7. Plot of Helmholtz free energy and the vibrational free energy (inset) for (a) $\text{Na}_4\text{P}_2\text{S}_6$ and (b) $\text{Li}_4\text{P}_2\text{S}_6$, comparing results for the $P\bar{3}m1$ (black), $C2/m$ (red), and the $P\bar{3}1m$ (purple) structures. In both sets of curves the zero of energy is taken by setting $U_{\text{SL}}(P\bar{3}m1) = 0$.

of these materials are substantial. For both materials at $T = 300$ K, the $C2/m$ structure has the lowest value of F_{vib} . This stabilizes the $\text{Na}_4\text{P}_2\text{S}_6$ in the $C2/m$ structure relative to the other two structures. However, for $\text{Li}_4\text{P}_2\text{S}_6$, the $P\bar{3}m1$ structure has the smallest value of $F = 0.19$ eV/formula unit benefiting from contributions of static lattice energy. Overall, our results on each material are consistent with the corresponding experimental analysis [6,7,11] in terms of structural stability.

In order to further understand how the phonon normal modes contribute to the vibrational Helmholtz free energy $F_{\text{vib}}(T)$, it is helpful to examine the weighted phonon density of states factor defined in Eq. (4) and its integral defined in Eq. (5) as well as the phonon density of states $g(\omega)$ defined by Eq. (6) which are all plotted in Fig. 8 for the functions evaluated at $T = 300$ K representing $\text{Na}_4\text{P}_2\text{S}_6$ (a) and $\text{Li}_4\text{P}_2\text{S}_6$ (b), both in their $C2/m$ structures. Here, we see that while $g(\omega) \geq 0$ for all frequencies ω , $f_{\text{vib}}(\omega, T)$ changes sign from negative to positive when $2 \sinh[\hbar\omega/(2k_B T)] = 1$. For $T = 300$ K, and for ω in units of cm^{-1} , this sign change occurs at

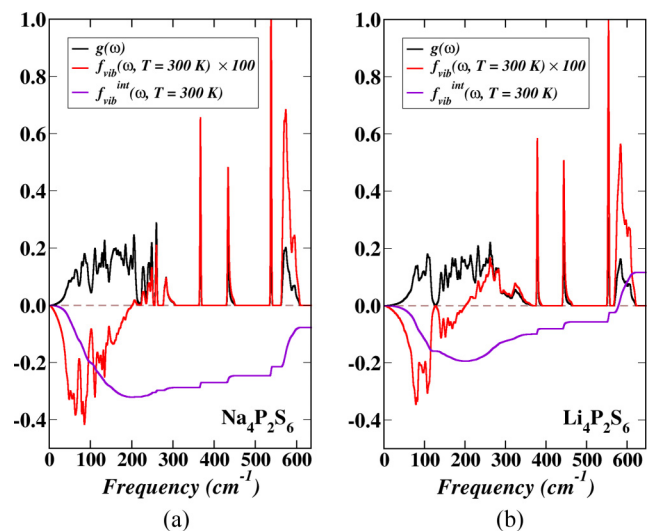


FIG. 8. Details of the vibrational stabilization at $T = 300$ K for (a) $\text{Na}_4\text{P}_2\text{S}_6$, (b) $\text{Li}_4\text{P}_2\text{S}_6$ in the $C2/m$ structure. In each subplot, the black curve indicates the phonon density of states $g(\omega)$, the red curve represents the weighted phonon density of states $f_{\text{vib}}(\omega, T = 300 \text{ K})$ scaled by a factor of 100, and the purple curve gives the integrated weighted phonon density of states factor $f_{\text{vib}}^{\text{int}}(\omega, T = 300 \text{ K})$ as defined in Eqs. (6), (4), and (5), respectively. In these plots the corresponding vertical scales are in units of states/ cm^{-1} for $g(\omega)$, eV/(formula unit)/ cm^{-1} for f_{vib} , and eV/(formula unit) for $f_{\text{vib}}^{\text{int}}$.

$\omega \approx 201 \text{ cm}^{-1}$. Figure 8 shows that in the frequency range $0 \leq \omega \leq 201 \text{ cm}^{-1}$, $\text{Na}_4\text{P}_2\text{S}_6$ has a greater phonon density of states than does $\text{Li}_4\text{P}_2\text{S}_6$, which numerically explains why the vibrational Helmholtz free energy of $\text{Na}_4\text{P}_2\text{S}_6$ is much lower than that of $\text{Li}_4\text{P}_2\text{S}_6$. Qualitatively, the fact that $\text{Na}_4\text{P}_2\text{S}_6$ has a greater phonon density of states at low frequencies could be explained by low-frequency vibrations of the more massive Na ions compared with those of the less massive Li ions.

IV. PREDICTION OF A MIXED-ION ELECTROLYTE $\text{Li}_2\text{Na}_2\text{P}_2\text{S}_6$

A. Optimized structure

In addition to the reexamination of known crystalline materials $\text{Na}_4\text{P}_2\text{S}_6$ and $\text{Li}_4\text{P}_2\text{S}_6$, we also examined the possibilities for mixed-ion material $\text{Li}_2\text{Na}_2\text{P}_2\text{S}_6$ based on the idea of ionic substitution. For example, starting with the $C2/m$ structure of crystalline $\text{Na}_4\text{P}_2\text{S}_6$, we consider the possibility of modifying the structure by substituting two Li ions for two Na ions in the setting of the primitive cell. The $C2/m$ structure of $\text{Na}_4\text{P}_2\text{S}_6$ has two crystallographically distinct Na sites with Wyckoff labels g and h . These are indicated by light blue and dark blue shades in Fig. 1(b), respectively. From this viewpoint, we intuitively construct two likely geometries of atomic arrangements for $\text{Li}_2\text{Na}_2\text{P}_2\text{S}_6$. For the configuration R_g^{Li} illustrated in Fig. 9(a), we replace all equivalent Na ions in $\text{Na}_4\text{P}_2\text{S}_6$ of type g with Li ions. For the configuration R_h^{Li} illustrated in Fig. 9(b), we replace all Na ions of type h with Li ions. After optimization using variable cell techniques, both proposed structures retain their space-group symmetry of

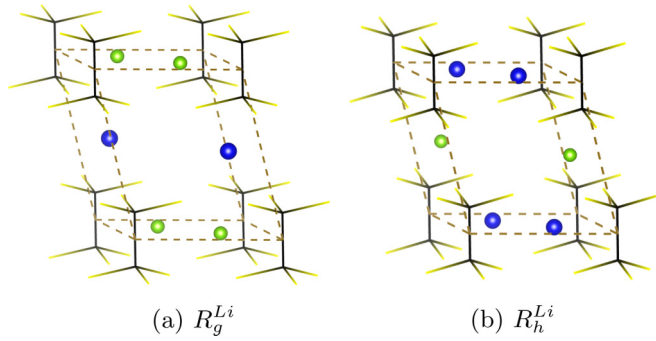


FIG. 9. Diagrams of two possible arrangements of ions for primitive crystalline unit cells of $\text{Li}_2\text{Na}_2\text{P}_2\text{S}_6$ in their optimized $C2/m$ structures with Li, Na, and the building block $(\text{P}_2\text{S}_6)^{4-}$ units represented by green balls, blue balls, and wire frames, respectively. Li ions in (a) are located at the equivalent g sites while in (b) Li ions are located at h sites.

$C2/m$ with the optimized lattice parameters for each potential structure being listed in Table III. Given that R_g^{Li} results in a low-energy structure having relative static lattice energy of -0.16 eV with respect to R_h^{Li} , this configuration is determined to be the ground structure of $\text{Li}_2\text{Na}_2\text{P}_2\text{S}_6$ and will be used in subsequent analysis and simulations. It is also worth mentioning that the equilibrium volume of $\text{Li}_2\text{Na}_2\text{P}_2\text{S}_6$ in the R_g^{Li} structure has approximately 10% less volume than that of $\text{Na}_4\text{P}_2\text{S}_6$, which is not surprising because the Li ion has a smaller radius than does the Na ion.

In the case of having Na as well as Li ions vibrating in the same lattice, it would be interesting to compare the vibrational features of $\text{Li}_2\text{Na}_2\text{P}_2\text{S}_6$ with those of the pure material $\text{Na}_4\text{P}_2\text{S}_6$ in terms of phonon dispersion relations which are given in Figs. 10 and 3(b), respectively. The comparison shows that the dispersion curves of the two materials are very similar with the same number of modes covering an almost identical range of frequencies. The fact that the harmonic phonon analysis of the ground-state structure of $\text{Li}_2\text{Na}_2\text{P}_2\text{S}_6$ results in all phonon modes having real frequencies, provides evidence of its dynamical stability.

TABLE III. Comparison of the optimized lattice parameters for $\text{Li}_2\text{Na}_2\text{P}_2\text{S}_6$ in the R_g^{Li} and R_h^{Li} structures. Also listed are the static lattice energy differences ΔU_{SL} referenced to the energy of the R_h^{Li} structure in units of eV/formula unit.

		R_g^{Li}	R_h^{Li}
Primitive cell:	$a = b$ (Å)	6.18	6.46
	c (Å)	7.50	7.01
	$\alpha = \beta$ (deg)	97.77	97.88
	γ (deg)	119.21	118.43
Conventional cell:	a_c (Å)	6.26	6.61
	b_c (Å)	10.67	11.10
	c_c (Å)	7.50	7.01
	β_c (deg)	105.50	105.54
	ΔU_{SL} (eV/FU)	-0.16	0.00

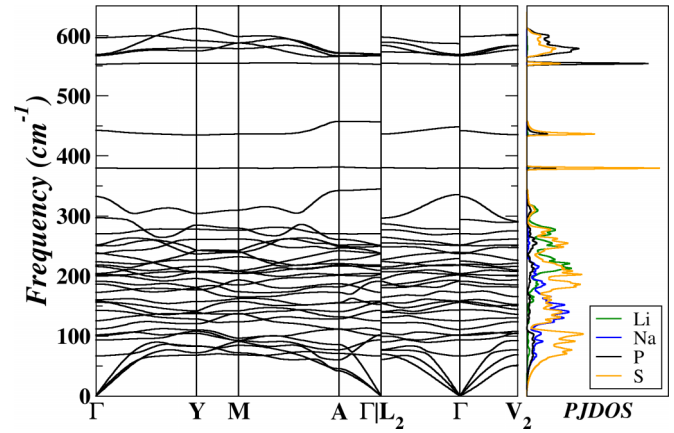
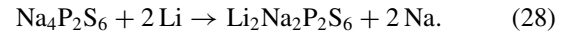


FIG. 10. Phonon band structure and the corresponding projected density of states for $\text{Li}_2\text{Na}_2\text{P}_2\text{S}_6$ (in the stable R_g^{Li} structure). See Fig. 3(e) for the Brillouin zone diagram of the $C2/m$ structure.

B. Possible reaction pathways

To the best of our knowledge, the crystal $\text{Li}_2\text{Na}_2\text{P}_2\text{S}_6$ has not been yet observed experimentally. However, with predictive capabilities of first-principles calculations, we can quantitatively evaluate the plausibility of synthesizing the material by considering a number of reactions. Perhaps the simplest reaction involves replacing Na with Li in $\text{Na}_4\text{P}_2\text{S}_6$ according to



In this reaction (28) we assume that both $\text{Na}_4\text{P}_2\text{S}_6$ and $\text{Li}_2\text{Na}_2\text{P}_2\text{S}_6$ are in their ground-state $C2/m$ structures and Li and Na are in their metallic body-centered-cubic structures. The reaction energy of the products P and the reactants R is then estimated from

$$\Delta F(T) = \Delta U_{\text{SL}} + \Delta F_{\text{vib}}(T) + \Delta F_{\text{elec}}^{\text{metal}}(T). \quad (29)$$

The reaction energy $\Delta F(T)$ calculated in this way represents the net energy of the process, typically referenced to room temperature ($T = 300$ K) and does not account for possible reaction barriers. Nevertheless, $\Delta F(T)$ is useful for assessing stabilities; $\Delta F(T) > 0$ implies that the reactants are more stable than the products, while $\Delta F(T) < 0$ implies that the products are more stable than the reactants at temperature T . Here, $\Delta U_{\text{SL}} = U_{\text{SL}}^{\text{P}} - U_{\text{SL}}^{\text{R}}$ represents the static lattice energy difference between the left-side reactants and the right-side products of the reaction as determined from ground-state (zero-temperature) density functional calculations. Similarly, we denote $\Delta F_{\text{vib}}(T) = F_{\text{vib}}^{\text{P}}(T) - F_{\text{vib}}^{\text{R}}(T)$ in the harmonic phonon approximation, as the vibrational energy change during the reaction process. For this reaction which involves metallic constituents, there is in principle a contribution $\Delta F_{\text{elec}}^{\text{metal}}(T)$ due to temperature-dependent electronic excitations of metallic Li and Na. However, our calculations indicate these contributions are numerically small ($\sim 10^{-3}$ eV) and can be neglected. Graphs of $\Delta F(T)$ and separately of the Helmholtz free energies of the reactants and products as a function of temperature T are presented in Fig. 11. For this reaction, $\Delta F(T) < 0$ for the computed temperature range and at $T = 300$ K, $\Delta F(T = 300 \text{ K}) = -0.35$ eV. This suggests

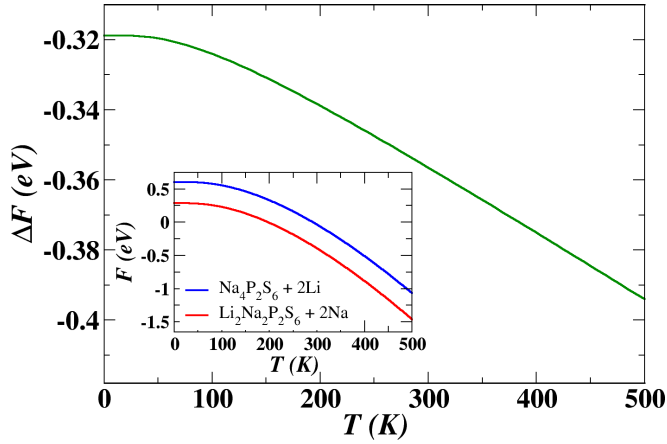


FIG. 11. Plot of the reaction energy of Eq. (28) as a function of temperature. The inner plot presents the comparison of the Helmholtz free energy of the reactants (blue curve) with that of products (red curve) for the predicted reaction.

that it is energetically favorable for Li to replace Na according to reaction (28) over a significant temperature range.

While reaction (28) provides a possible synthesis route producing the mixed-ion electrolyte with an excess Na metal coating, there are a number of other possible reactions one can imagine to produce the pure mixed-ion electrolyte $\text{Li}_2\text{Na}_2\text{P}_2\text{S}_6$. We have analyzed some of these according to Eq. (29), neglecting the $\Delta F_{\text{elec}}^{\text{metal}}(T)$ contributions. The results are summarized together with the results for reaction [(28) or No. 1] in Table IV. From this table, we see that the only reaction that has a positive ΔF is No. 3, suggesting that $\text{Li}_2\text{Na}_2\text{P}_2\text{S}_6$ is unstable relative to the phase-separated mixture of $\text{Na}_4\text{P}_2\text{S}_6$ and $\text{Li}_4\text{P}_2\text{S}_6$. On the other hand, knowing that $\text{Li}_4\text{P}_2\text{S}_6$ forms at very high temperature [2,7,9] suggests that there may be a large activation barrier to the formation of $\text{Li}_4\text{P}_2\text{S}_6$. It is possible that a low-temperature synthesis process that keeps the reaction energy below the energy of the

reaction barrier to form $\text{Li}_4\text{P}_2\text{S}_6$ could provide a successful pathway to the synthesis of $\text{Li}_2\text{Na}_2\text{P}_2\text{S}_6$. Perhaps some of the reactions mentioned in Table IV (other than No. 3) are worth investigating for this purpose.

V. IONIC CONDUCTIVITIES

A. Nudged elastic band (NEB) analysis

In order to understand mechanisms of Na ion conductivity in $\text{Na}_4\text{P}_2\text{S}_6$ and $\text{Li}_2\text{Na}_2\text{P}_2\text{S}_6$ in the $C2/m$ structure, it is helpful to visualize part of simulation cell (composed of $2 \times 1 \times 2$ conventional monoclinic cells) as illustrated in Fig. 12(a). Previously reported analysis of Na ion conductivity in $\text{Na}_4\text{P}_2\text{S}_6$ in the $C2/m$ structure [8] found the most energetically favorable migration to occur with a vacancy mechanism within planes containing Na ions at the crystallographic h sites between $(\text{P}_2\text{S}_6)^{4-}$ layers. One example zigzag path is illustrated in Fig. 12(a) showing net migration along the \mathbf{a} axis. Using the NEB methods discussed in Sec. II C1, the energy path diagrams for Na ion vacancy migration along neighboring h sites for $\text{Na}_4\text{P}_2\text{S}_6$ and $\text{Li}_2\text{Na}_2\text{P}_2\text{S}_6$ are compared in Fig. 12(b). The results indicate that E_m is significantly smaller for $\text{Li}_2\text{Na}_2\text{P}_2\text{S}_6$ compared with that of $\text{Na}_4\text{P}_2\text{S}_6$ which correlates with the shortened distance between neighboring h sites by approximately 0.2 Å.

The Na ion vacancy mechanism for the macroscopic ion conductivity depends upon a population of Na ion vacancies. For a highly ordered crystal, this population depends on the “formation” of interstitial-vacancy pairs. In previous work [8], the most favorable interstitial sites were found to be located at the crystallographic d sites which are close to and in the same plane as the h sites as shown in Fig. 12(a). The results of this work using the PBEsol exchange-correlation function are qualitatively similar but numerically different from the previous work [8] which used the LDA functional. In this work, we find the following values (in units of eV): $E_m = 0.25$ and 0.16 and $E_f = 0.18$ and 0.13 for $\text{Na}_4\text{P}_2\text{S}_6$ and $\text{Li}_2\text{Na}_2\text{P}_2\text{S}_6$, respectively, suggesting that $\text{Li}_2\text{Na}_2\text{P}_2\text{S}_6$ may

TABLE IV. Computed energy differences [Eq. (29)] for indicated reactions in eV units, evaluated at $T = 300$ K and neglecting electronic excitation contributions. $\text{Na}_4\text{P}_2\text{S}_6$ and $\text{Li}_2\text{Na}_2\text{P}_2\text{S}_6$ are assumed to have the optimized $C2/m$ structures discussed in this paper, $\text{Li}_4\text{P}_2\text{S}_6$ is assumed to have the optimized $P\bar{3}m1$ structure discussed in this paper, Na and Li are assumed to have the optimized bcc [space group $Im\bar{3}m$ (No. 229)] structures, while the assumed structures of all other constituents are referenced in the footnotes.

No.	Reaction: $R \rightarrow P$	ΔU_{SL}	ΔF_{vib}	ΔF
1	$\text{Na}_4\text{P}_2\text{S}_6 + 2 \text{Li} \rightarrow \text{Li}_2\text{Na}_2\text{P}_2\text{S}_6 + 2 \text{Na}$	-0.29	-0.06	-0.35
2	$2 \text{Li} + 2 \text{Na} + 2 \text{P}^{\text{a}} + 6 \text{S}^{\text{b}} \rightarrow \text{Li}_2\text{Na}_2\text{P}_2\text{S}_6$	-10.62	0.06	-10.56
3	$\frac{1}{2} \text{Na}_4\text{P}_2\text{S}_6 + \frac{1}{2} \text{Li}_4\text{P}_2\text{S}_6 \rightarrow \text{Li}_2\text{Na}_2\text{P}_2\text{S}_6$	0.13	-0.03	0.10
4	$\frac{1}{2} \text{Na}_4\text{P}_2\text{S}_6 + \frac{2}{3} \text{Li}_3\text{PS}_4^{\text{c}} + \frac{1}{12} \text{P}_4\text{S}_4^{\text{d}} \rightarrow \text{Li}_2\text{Na}_2\text{P}_2\text{S}_6$	-0.24	-0.02	-0.26
5	$\frac{2}{3} \text{Na}_3\text{PS}_4^{\text{e}} + \frac{2}{3} \text{Li}_3\text{PS}_4^{\text{c}} + \frac{1}{6} \text{P}_4\text{S}_4^{\text{d}} \rightarrow \text{Li}_2\text{Na}_2\text{P}_2\text{S}_6$	-0.48	-0.00	-0.48
6	$\frac{2}{3} \text{Na}_3\text{PS}_4^{\text{e}} + \frac{1}{3} \text{P}_4\text{S}_{10}^{\text{f}} + 2 \text{Li} \rightarrow \text{Li}_2\text{Na}_2\text{P}_2\text{S}_6$	-5.01	0.06	-4.95
7	$\frac{2}{3} \text{Li}_3\text{PS}_4^{\text{c}} + \frac{1}{3} \text{P}_4\text{S}_{10}^{\text{f}} + 2 \text{Na} \rightarrow \text{Li}_2\text{Na}_2\text{P}_2\text{S}_6$	-4.70	0.07	-4.63

^aBlack phosphorous with space group $Cmce$ (No. 64); from Ref. [59].

^bOrthorhombic (α - S_8) with space group $Fddd$ (No. 70); from Ref. [60].

^c γ - Li_3PS_4 with space group $Pmn2_1$ (No. 31); from Ref. [61].

^d α - P_4S_4 with space group $C2/c$ (No. 15); from Ref. [62].

^e α - Na_3PS_4 with space group $P\bar{4}2_1c$ (No. 114); from Ref. [63].

^f P_4S_{10} with space group $P\bar{1}$ (No. 2); from Ref. [64].

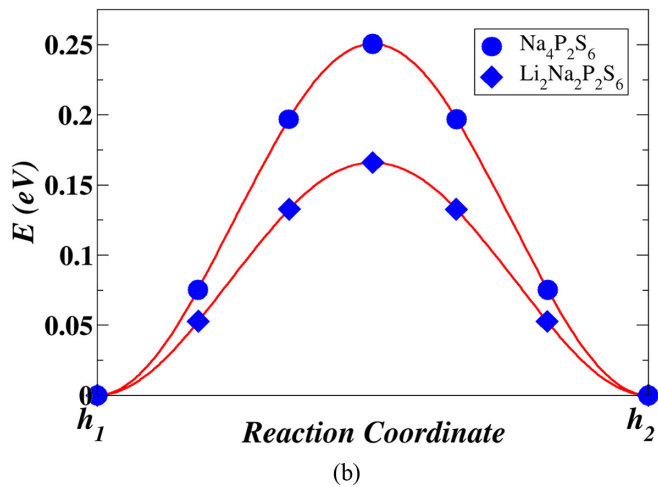
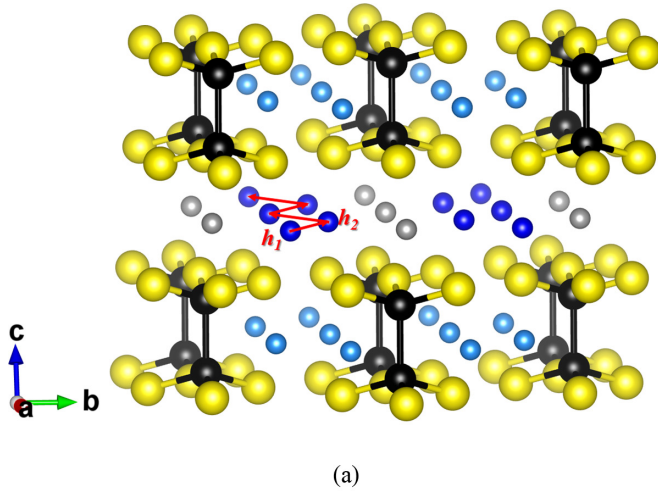


FIG. 12. (a) Ball and stick diagram of a portion of the simulation cell used to study Na ion conductivity in $\text{Na}_4\text{P}_2\text{S}_6$ and $\text{Li}_2\text{Na}_2\text{P}_2\text{S}_6$ with the same ball color conventions as used in the diagrams shown in Sec. III. Dark blue balls indicate Na ions with Wyckoff labels h , light blue balls indicate Na or Li ions with Wyckoff labels g , and gray balls indicate interstitial sites with Wyckoff labels d . The red arrows indicate the most likely Na ion vacancy migration pathway between adjacent h sites. (b) Configuration energy diagram results of NEB calculation of Na ion vacancy migration along one step of the indicated pathway, comparing results for $\text{Na}_4\text{P}_2\text{S}_6$ and $\text{Li}_2\text{Na}_2\text{P}_2\text{S}_6$.

have promising Na ion conductivity. These and related results will be summarized in Table V.

B. Molecular dynamics simulations

First-principles molecular dynamics simulations were performed using supercells of $\text{Na}_4\text{P}_2\text{S}_6$ and $\text{Li}_2\text{Na}_2\text{P}_2\text{S}_6$ as described in Sec. IIC2. In order to collect statistically significant numbers of hopping events within reasonable simulation times, it was necessary to use high temperatures for the simulations; typically the temperature averaged over the simulation time was $\langle T \rangle > 900$ K. It is expected that the high-temperature simulation results can be extrapolated to more physical temperatures in a simplified accelerated dynamics

TABLE V. NEB and MD results on $\text{Na}_4\text{P}_2\text{S}_6$ and $\text{Li}_2\text{Na}_2\text{P}_2\text{S}_6$ calculated with the PBEsol exchange-correlation functional, in comparison to those of previous work obtained using the LDA exchange-correlation functional and available experimental data. All energies are given in eV units.

Materials	Analysis	E_m	E_f	E_a
$\text{Na}_4\text{P}_2\text{S}_6$	LDA + NEB ^a	0.30	0.24	0.42
	PBEsol + NEB	0.25	0.18	0.34
	PBEsol + MD			0.41
	Experiment ^b			0.39
$\text{Li}_2\text{Na}_2\text{P}_2\text{S}_6$	PBEsol + NEB	0.16	0.13	0.23
	PBEsol + MD			0.30

^aReference [8].

^bReference [6].

algorithm [65]. This approach follows the pioneering work of Mo *et al.* [66].

The results offer additional perspectives on the Na ion migration mechanisms of these materials. In particular, by directly observing the ion trajectories, we find that the most significant ion motion occurs within planes containing Na ions (located at the Wyckoff labeled h sites at equilibrium) between $(\text{P}_2\text{S}_6)^{4-}$ layers, consistent with the NEB analysis discussed above. For simplicity, we will refer to this plane as the interlayer plane. We found that there is essentially no conduction path along the c axis of these materials. We also examined the Li ion motion for $\text{Li}_2\text{Na}_2\text{P}_2\text{S}_6$. At equilibrium, the ions are located at the Wyckoff sites labeled g which are within the $(\text{P}_2\text{S}_6)^{4-}$ layer planes. We found the Li ion trajectories to be characterized by oscillations about their equilibrium positions resulting in a high degree of site localization and essentially no diffusion. Similar behavior was observed for the g -site Na ions in $\text{Na}_4\text{P}_2\text{S}_6$.

In order to visualize the significant Na ion motion in these materials, Fig. 13 shows the superposed snapshots of the ion positions in a volume containing the interlayer plane. The snapshots were taken each time interval of $20\Delta t$, where Δt denotes the Verlet time integration parameter, for the first 30 ps of the MD simulations. For $\text{Na}_4\text{P}_2\text{S}_6$ the average temperature was $\langle T \rangle = 955$ K and for $\text{Li}_2\text{Na}_2\text{P}_2\text{S}_6$ the average temperature was $\langle T \rangle = 973$ K. At the beginning of the calculation, there are eight Na ions with labels from Na(1) to Na(8) corresponding to their respective host lattice h sites ($h_1 - h_8$) in the simulation cell. The notations ($d_1 - d_4$) indicate the interstitial d sites within the supercell. More labels with superscript “prime” were placed in each subfigure representing sites in neighboring cells.

Figure 13 shows that in contrast to the predictions of the NEB analysis which focused on ion vacancy migration along the a axis, the molecular dynamics results suggest that ion migration occurs throughout the interlayer plane due to involvement of the interstitial d sites. Additionally, the results qualitatively show that, compared to the case for $\text{Na}_4\text{P}_2\text{S}_6$, it is evident that the Na ions hop more frequently in $\text{Li}_2\text{Na}_2\text{P}_2\text{S}_6$, presenting a more extensive network of diffusional channels. Some general observations of the hopping events are as follows. The migration of Na ions is either via direct vacancy

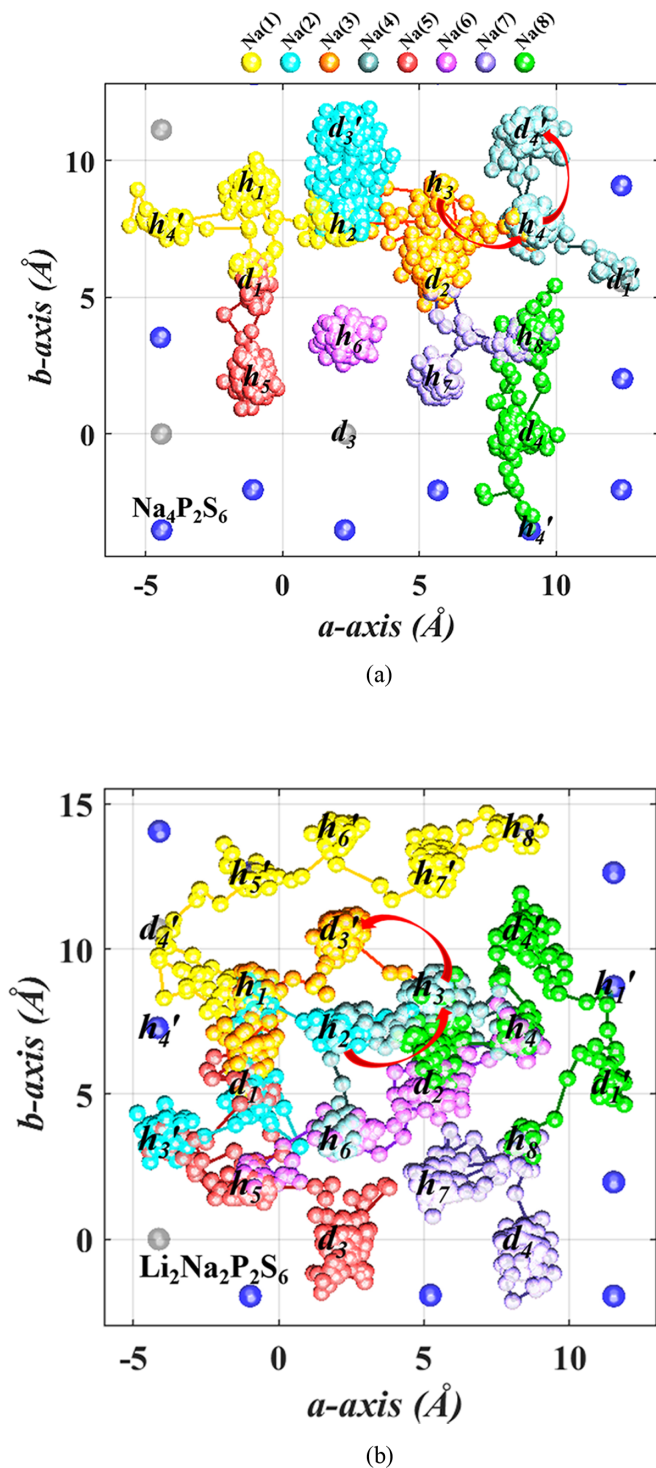


FIG. 13. Superposed snapshots of 30-ps molecular dynamics simulations visualized within slices of the simulation cells containing an interlayer plane for (a) $\text{Na}_4\text{P}_2\text{S}_6$ with average temperature $\langle T \rangle = 955$ K and (b) $\text{Li}_2\text{Na}_2\text{P}_2\text{S}_6$ with average temperature $\langle T \rangle = 973$ K. The time interval between snapshots is $20\Delta t = 0.048$ ps. The blue balls represent the host h sites and the gray balls represent the interstitial d sites. Each distinct Na ion is represented with a unique color in order to follow its motion throughout the simulation. The red arrows indicate particular examples of Na ion jumps between sites with the tail and head of each arrow consistent with the time sequence of the jump.

mechanism between the host $h \leftrightarrow h$ sites or via indirect vacancy mechanism between $h \leftrightarrow d$ sites. Specifically, the diffusion process can be triggered by one Na ion at a host h site jumping into the nearest-neighbor d site, leaving a vacancy that is available to be occupied by another Na ion from a nearby h site. For these simulations, no migrations between the $d \leftrightarrow d$ sites were observed. This suggests that for these materials, the Na ion migration processes involve both direct vacancy hops and indirect vacancy hops with interstitial intermediates, but direct interstitial mechanisms were not identified in these data sets. For example, in Fig. 13(a) the first hop in the simulation occurs for Na(4) at $t = 0.60$ ps, jumping from site h_4 to site d'_4 . Later at $t = 1.57$ ps, the Na(3) ion jumps from site h_3 to fill the vacancy h_4 . A similar initial process is observed in Fig. 13(b) in a faster timescale where $t = 0.60$ ps, the Na(3) ion jumps from site h_3 into the site d'_3 , and subsequently at $t = 0.97$ ps, the Na(2) ion jumps from its h_2 site into the vacant h_3 site.

In order to quantify these effects, we can analyze the nearest-neighbor hopping events as a function of time. In particular, for $t > 0$, we can determine the average number of hops between nearest-neighbor (nn) h sites [$H_{h \leftrightarrow h}(t)$] and the average number of hops between nearest-neighbor (nn) $h \leftrightarrow d$ sites [$H_{h \leftrightarrow d}(t)$] in the following way. Within the simulation cell there are 2 interlayer planes containing a total of 16 Na ions, each with a label s . At each time t , we assign each of these s mobile ions to the nearest host lattice site h_k where within each plane, $1 \leq k \leq 8$ or interstitial site d_l where within each plane $1 \leq l \leq 4$. Then, for each time $t > 0$, we compute the hop counter functions according to the comparison of the site assignments at time $t - \Delta t$ and t :

$$C_{h \leftrightarrow h}^s(t) = \begin{cases} C_{h \leftrightarrow h}^s(t - \Delta t), & \text{no config. change} \\ C_{h \leftrightarrow h}^s(t - \Delta t) + 1, & h \leftrightarrow \text{nn } h \end{cases} \quad (30)$$

$$C_{h \leftrightarrow d}^s(t) = \begin{cases} C_{h \leftrightarrow d}^s(t - \Delta t), & \text{no config. change} \\ C_{h \leftrightarrow d}^s(t - \Delta t) + 1, & \{h, d\} \leftrightarrow \text{nn } \{d, h\} \end{cases}$$

with $C_{h \leftrightarrow h}^s(t = 0) = 0 = C_{h \leftrightarrow d}^s(t = 0)$. The algorithm must be adapted to take into account hops across the simulation cell boundaries. From these hop counter results we can then compute the accumulated and averaged hop functions according to

$$H_{h \leftrightarrow h}(t) = \frac{1}{16} \sum_{s=1}^{16} C_{h \leftrightarrow h}^s(t),$$

$$H_{h \leftrightarrow d}(t) = \frac{1}{16} \sum_{s=1}^{16} C_{h \leftrightarrow d}^s(t). \quad (31)$$

The results of this analysis are illustrated in Fig. 14. As expected, the accumulated hop function for $\text{Li}_2\text{Na}_2\text{P}_2\text{S}_6$ is larger than the corresponding function for $\text{Na}_4\text{P}_2\text{S}_6$ for both $h \leftrightarrow d$ and $h \leftrightarrow h$ events. A less intuitive result of this analysis is that $H_{h \leftrightarrow d}(t) > H_{h \leftrightarrow h}(t)$ for both materials, indicating the importance of the intermediate interstitial processes for ion migration in these materials.

In order to connect the simulations with ion conductivity, molecular dynamics runs with simulation times of 50–70 ps were performed at various average temperatures. For $\text{Na}_4\text{P}_2\text{S}_6$ the average temperatures were $\langle T \rangle = 955, 1051, 1143$, and

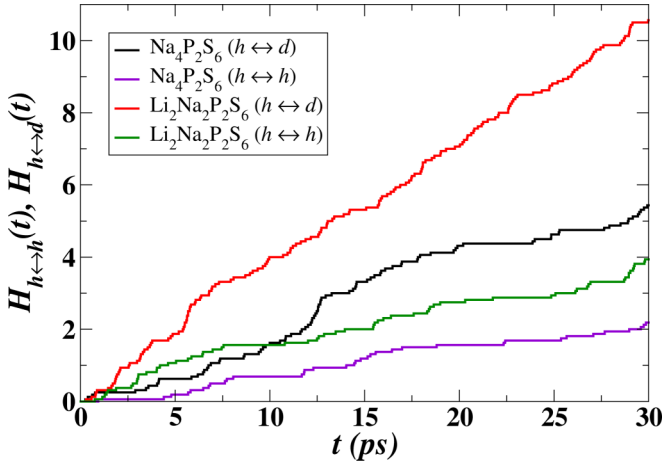


FIG. 14. Plots of the accumulated hop functions $H_{h \leftrightarrow h}(t)$ and $H_{h \leftrightarrow d}(t)$ as a function of the simulation time t . The results for $\text{Na}_4\text{P}_2\text{S}_6$ are shown in black and purple and the results for $\text{Li}_2\text{Na}_2\text{P}_2\text{S}_6$ are shown in red and green. The data from the simulations illustrated in Fig. 13 were used for this analysis.

1287 K, while for $\text{Li}_2\text{Na}_2\text{P}_2\text{S}_6$ the average temperatures were $\langle T \rangle = 994, 1060, 1193,$ and 1260 K. The results, assuming the Haven ratio $H_r = 1$, together with the available experimental measurements are presented in Fig. 15, plotting $\log(T\sigma)$ vs $1/T$. On the basis of Eqs. (24) and (25), the activation energy is obtained from the slope of the corresponding fit line. For the case of $\text{Na}_4\text{P}_2\text{S}_6$, it shows that the calculated tracer activation energy $E_a^{\text{MSD}} = 0.41$ eV is in reasonably good agreement with the experimental value of $E_a^{\text{expt}} = 0.39$ eV. The discrepancy between experiment and computation may be due to the rough approximation of the Haven ratio. Other possible reasons for the discrepancy include the choice of statistical ensemble for modeling the system and the simulation time may also affect the accuracy

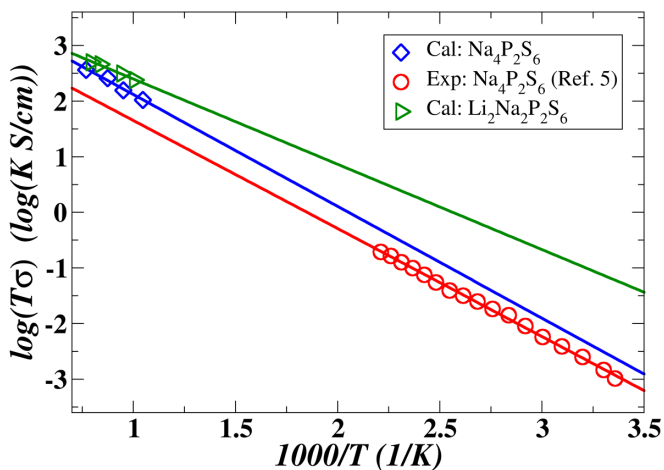


FIG. 15. Plots of the ionic conductivity with the calculated values for $\text{Na}_4\text{P}_2\text{S}_6$ (blue diamonds) and $\text{Li}_2\text{Na}_2\text{P}_2\text{S}_6$ (green triangles) evaluated using Eq. (25) with $H_r = 1$. The experimental value for $\text{Na}_4\text{P}_2\text{S}_6$ (red circles) was obtained by refitting the data in Ref. [6]. The straight lines represent the best fit of the computational or the experimental analysis.

of the numerical analysis. The tracer activation energy of $\text{Li}_2\text{Na}_2\text{P}_2\text{S}_6$ is $E_a^{\text{MSD}} = 0.30$ eV. Consistent with the NEB analysis, we again see that $\text{Li}_2\text{Na}_2\text{P}_2\text{S}_6$ presents better ionic conductivity than $\text{Na}_4\text{P}_2\text{S}_6$. The results for both NEB and molecular dynamics analyses are summarized in Table V. Here, we note that for these systems, $E_a^{\text{NEB}} \neq E_a^{\text{MSD}}$ because of their different treatments of the effects of interstitial (d) sites. The NEB analysis presented here only considered direct hops between nearest-neighbor vacancy sites, including the interstitial sites only in the estimation of the population of vacancies via the Boltzmann factor due to the formation energy E_f of the interstitial-vacancy pair. The molecular dynamics analyses indicate significant contributions of hops between vacancy and interstitial sites, presenting a plausibly more physical picture of the Na ion migration processes.

VI. DISCUSSION AND CONCLUSIONS

The three focuses of this work are (1) a comprehensive (re)examination of the crystal structures and stabilities of $\text{Li}_4\text{P}_2\text{S}_6$ and $\text{Na}_4\text{P}_2\text{S}_6$, (2) a prediction and analysis of a mixed-ion electrolyte $\text{Li}_2\text{Na}_2\text{P}_2\text{S}_6$, and (3) an assessment of the Na ion conductivity properties of $\text{Na}_4\text{P}_2\text{S}_6$ and of the mixed-ion material $\text{Li}_2\text{Na}_2\text{P}_2\text{S}_6$.

The results of the structural analyses are presented in Sec. III with the numerical results evaluated at $T = 300$ K summarized in Table II. Here we see that, within the harmonic phonon approximation [14,35], the Helmholtz free energy due to vibrations plays a nontrivial role in stabilizing the materials. Using plots of the weighted phonon density of states factor and its integral in Fig. 8, it is possible to understand the vibrational stabilization of the more massive Na ions relative to the corresponding Li ion vibrations in these materials. Additionally, we found that computations using the PBEsol exchange-correlation functional [33] contributed to the better agreement with the experimental results compared with previous calculations [2,8] which used the LDA exchange-correlation functional [29]. The present computational results are consistent with the latest structural analyses, finding the stable structures at $T = 300$ K to be the Neuberger structure [7] for $\text{Li}_4\text{P}_2\text{S}_6$ and the Kuhn structure [11] for $\text{Na}_4\text{P}_2\text{S}_6$. For the Neuberger structure, we offered computational evidence of a slight correction to structural analysis, suggesting that the space group should be $P3m1$ (No. 164) rather than the reported space group of $P321$. Further evidence of computational consistency with experiment was obtained in comparing experimental and computational nonresonant Raman phonon spectra of $\text{Na}_4\text{P}_2\text{S}_6$ shown in Fig. 4. Here, the most intense signal was identified as due to the internal stretching mode of the $(\text{P}_2\text{S}_6)^{4-}$ complex ions.

The results of analyzing the structure and stability of the possible mixed-ion electrolyte $\text{Li}_2\text{Na}_2\text{P}_2\text{S}_6$ are presented in Sec. IV. We found that two Li ions can substitute for the two intralayer Na ions of $\text{Na}_4\text{P}_2\text{S}_6$ in the $C2/m$ structure. Here, “intralayer” refers to the layers containing the $(\text{P}_2\text{S}_6)^{4-}$ building blocks of the structure. Compared with the original $\text{Na}_4\text{P}_2\text{S}_6$ structure, the resulting $\text{Li}_2\text{Na}_2\text{P}_2\text{S}_6$ crystal maintains the $C2/m$ space group with contracted lattice constants in the layer planes. Both $\text{Na}_4\text{P}_2\text{S}_6$ and $\text{Li}_2\text{Na}_2\text{P}_2\text{S}_6$ have similar interlayer Na ions arranged at equilibrium on sites with Wyckoff

TABLE VI. Comparison of the fractional coordinates of Li/Na₄P₂S₆ based on the Neuberger structure [7]. The column labeled “Wyck” lists the conventional cell multiplicity and Wyckoff labels based on the $P\bar{3}m1$ space group. The “Experiment” column lists the coordinates from the $P321$ analysis [7] which in general is in one-to-one correspondence except that the 6g sites of the $P\bar{3}m1$ structure map to two distinct $3e$ sites of the $P321$ structure and $6h$ sites of the $P\bar{3}m1$ structure map to two distinct $3f$ sites of the $P321$ structure as indicated.

Li ₄ P ₂ S ₆		Calculated			Experiment		
Atom	Wyck	x	y	z	x	y	z
Li	6 g	0.666	0.000	0.000	0.625/−0.683	0.000	0.0000
Li	6 h	0.667	0.000	$\frac{1}{2}$	0.631/−0.671	0.000	$\frac{1}{2}$
P	2 c	0.000	0.000	0.171	0.000	0.000	0.170
P	2 d	$\frac{1}{3}$	$\frac{2}{3}$	0.663	$\frac{1}{3}$	$\frac{2}{3}$	0.668
P	2 d	$\frac{1}{3}$	$\frac{2}{3}$	0.324	$\frac{1}{3}$	$\frac{2}{3}$	0.335
S	6 i	0.110	0.220	0.242	0.108	0.217	0.241
S	6 i	0.114	0.557	0.254	0.122	0.561	0.250
S	6 i	0.447	0.224	0.259	0.452	0.226	0.255
Na ₄ P ₂ S ₆		Calculated			Experiment		
Atom	Wyck	x	y	z	x	y	z
Na	6 g	0.659	0.000	0.000			
Na	6 h	0.676	0.000	$\frac{1}{2}$			
P	2 c	0.000	0.000	0.157			
P	2 d	$\frac{1}{3}$	$\frac{2}{3}$	0.660			
P	2 d	$\frac{1}{3}$	$\frac{2}{3}$	0.342			
S	6 i	0.102	0.205	0.229			
S	6 i	0.129	0.564	0.271			
S	6 i	0.463	0.231	0.264			

label h . Table IV lists reaction energies as estimated from differences in the Helmholtz free energies in the harmonic phonon approximation evaluated at $T = 300$ K for several possible reaction pathways. While we find that Li₂Na₂P₂S₆ is unstable with respect to $\frac{1}{2}(\text{Li}_4\text{P}_2\text{S}_6 + \text{Na}_4\text{P}_2\text{S}_6)$, we reasonably argue that since Li₄P₂S₆ forms at high temperature (typically 900°C) [2,7,9], it may be possible to stabilize

Li₂Na₂P₂S₆ with low-temperature reactions such as perhaps some of those listed in Table IV.

Results relating to simulations of Na ion conductivity in Na₄P₂S₆ and Li₂Na₂P₂S₆ are presented in Sec. V. Both NEB and molecular dynamics simulations find the dominant ionic conductivity to be due to Na ion motions in the interlayer planes. Because of its contracted lattice, it is predicted that

TABLE VII. Calculated fractional atomic coordinates of Li/Na₄P₂S₆ in the Kuhn structure [11] based on the conventional unit cell compared with the Kuhn structure [11] listed in the “Experiment” column. The column labeled “Wyck” lists the conventional cell multiplicity and Wyckoff label.

Li ₄ P ₂ S ₆		Calculated			Experiment		
Atom	Wyck	x	y	z	x	y	z
Li	4 g	0.000	0.668	0.000			
Li	4 h	0.000	0.823	0.500			
P	4 i	0.055	0.000	0.168			
S	4 i	0.769	0.000	0.260			
S	8 j	0.734	0.336	0.238			
Na ₄ P ₂ S ₆		Calculated			Experiment		
Atom	Wyck	x	y	z	x	y	z
Na	4 g	0.000	0.662	0.000	0.0000	0.6627	0.0000
Na	4 h	0.000	0.816	0.500	0.0000	0.8153	0.5000
P	4 i	0.053	0.000	0.157	0.0532	0.0000	0.1561
S	4 i	0.794	0.000	0.244	0.7942	0.0000	0.2414
S	8 j	0.722	0.347	0.230	0.7233	0.3499	0.2312

TABLE VIII. Fractional coordinates of Li/Na₄P₂S₆ simulated in the $P\bar{3}1m$ structure. The column labeled “Wyck” lists the conventional cell multiplicity and Wyckoff label.

Atom	Wyck	Li ₄ P ₂ S ₆			Na ₄ P ₂ S ₆		
		x	y	z	x	y	z
Li/Na	2 c	$\frac{1}{3}$	$\frac{2}{3}$	0.000	$\frac{1}{3}$	$\frac{2}{3}$	0.000
Li/Na	2 d	$\frac{1}{3}$	$\frac{2}{3}$	$\frac{1}{2}$	$\frac{1}{3}$	$\frac{2}{3}$	$\frac{1}{2}$
P	2 e	0.000	0.000	0.174	0.000	0.000	0.163
S	6 k	0.329	0.000	0.247	0.304	0.000	0.238

Li₂Na₂P₂S₆ has larger conductivity and lower activation barriers compared with Na₄P₂S₆. The analysis of the molecular dynamics trajectories suggests that both Na ion vacancy migration and indirect participation of interstitial sites contribute to the conductivity throughout the interlayer plane. Analyzing the Na ion trajectories in terms of the MSD(t , T) [Eq. (23)] and using the Nernst-Einstein equation (25) with the assumption of the Haven ratio $H_r = 1$, the simulated ion conductivity could be compared with the experimental measurements for Na₄P₂S₆ as shown in Fig. 15. There is reasonable agreement between the simulations and experimental results. If it becomes possible to stabilize the mixed-ion material Li₂Na₂P₂S₆, our simulations suggest that it will have a very promising Na ion conductivity.

ACKNOWLEDGMENTS

This work was supported by NSF Grant No. DMR-1507942. Computations were performed on the Wake Forest University DEAC cluster, a centrally managed resource with support provided in part by the University. Helpful discussions with A. Lachgar and D. Kondipudi from the WFU Department of Chemistry are gratefully acknowledged. Experimental work was conducted at the Center for Nanophase Materials Sciences, which is a Department of Energy Office of Science User Facility.

APPENDIX A: DETAILS OF THE NEUBERGER STRUCTURES OF Li₄P₂S₆ AND Na₄P₂S₆

The simulated structure corresponding to the structure analyzed by Neuberger [7] is detailed in Table VI. We use the space-group analysis of the $P\bar{3}1m$ structure rather than of the $P321$ structure of the Neuberger paper [7]. The P positions for the two space groups have the same Wyckoff labels, while the S positions of the $P321$ structure having the 6g multiplicity and label are equivalent to the 6i multiplicity and label of the $P\bar{3}1m$ structure. For the Li/Na sites, the pairs of 3e and 3f sites of the $P321$ structure correspond to the 6g and 6h multiplicities and labels of the $P\bar{3}1m$ structure.

APPENDIX B: DETAILS OF KUHN STRUCTURES OF Li₄P₂S₆ AND Na₄P₂S₆

The simulated fractional atomic coordinates of Li₄P₂S₆ and Na₄P₂S₆ are detailed in Table VII based on the conventional unit cell in the $C2/m$ structure and compared with the experimental results reported by Ref. [11] from x-ray

measurements on single-crystal samples. The results are very similar to those reported earlier by Rush *et al.* [8] simulated using the LDA exchange-correlation functional.

APPENDIX C: DETAILS OF THE $P\bar{3}1m$ REFERENCE STRUCTURES OF Li₄P₂S₆ AND Na₄P₂S₆

Table VIII lists the fractional coordinates of Li/Na₄P₂S₆ found in these simulations for the metastable $P\bar{3}1m$ structure. The corresponding lattice parameters are listed in Table I and the results are very similar to those reported earlier by Rush *et al.* [8] simulated using the LDA exchange-correlation functional.

APPENDIX D: DETAILS OF THE PREDICTED STRUCTURE OF CRYSTALLINE Li₂Na₂P₂S₆

Table IX lists the fractional coordinates of Li₂Na₂P₂S₆ for the ground-state R_g^{Li} structure in comparison with the results for the metastable R_h^{Li} structure. The initial configurations of these two structures were constructed based on the optimized primitive cell parameters of Kuhn structure for Na₄P₂S₆.

TABLE IX. Calculated fractional coordinates of Li₂Na₂P₂S₆ in the R_g^{Li} and the R_h^{Li} structures based on the conventional unit cell of $C2/m$ symmetry. The column labeled “Wyck” lists the conventional cell multiplicity and Wyckoff label.

Li ₂ Na ₂ P ₂ S ₆		R_g^{Li}		
Atom	Wyck	x	y	z
Li	4 g	0.000	0.668	0.000
Na	4 h	0.000	0.817	0.500
P	4 i	0.053	0.000	0.154
S	4 i	0.768	0.000	0.236
S	8 j	0.732	0.339	0.217
Li ₂ Na ₂ P ₂ S ₆		R_h^{Li}		
Atom	Wyck	x	y	z
Li	4 h	0.000	0.843	0.500
Na	4 g	0.000	0.664	0.000
P	4 i	0.052	0.000	0.167
S	4 i	0.786	0.000	0.263
S	8 j	0.718	0.346	0.251

- [1] T. Famprakis, P. Canepa, J. A. Dawson, M. S. Islam, and C. Masquelier, *Nat. Mater.* **18**, 1278 (2019).
- [2] Z. D. Hood, C. Kates, M. Kirkham, S. Adhikari, C. Liang, and N. A. W. Holzwarth, *Solid State Ionics* **284**, 61 (2016).
- [3] C. Dietrich, M. Sadowski, S. Siculo, D. A. Weber, S. J. Sedlmaier, K. S. Weldert, S. Indris, K. Albe, J. Janek, and W. G. Zeier, *Chem. Mater.* **28**, 8764 (2016).
- [4] Ö. U. Kudu, T. Famprakis, B. Fleutot, M.-D. Braida, T. Le Mercier, M. S. Islam, and C. Masquelier, *J. Power Sources* **407**, 31 (2018).
- [5] K. Minami, A. Hayashi, and M. Tatsumisago, *J. Ceram. Soc. Jpn.* **118**, 305 (2010).
- [6] Z. D. Hood, H. Wang, X. Liu, A. S. Pandian, R. Peng, J. K. Keum, and M. Chi (unpublished).
- [7] S. Neuberger, S. P. Culver, H. Eckert, W. G. Zeier, and J. Schmedt auf der Günne, *Dalton Trans.* **47**, 11691 (2018).
- [8] L. E. Rush Jr. and N. A. W. Holzwarth, *Solid State Ionics* **286**, 45 (2016).
- [9] R. Mercier, J. P. Malugani, B. Fahys, J. Douglanle, and G. Robert, *J. Solid State Chem.* **43**, 151 (1982).
- [10] *International Tables for Crystallography, Volume A: Space-group symmetry, Fifth revised edition*, edited by T. Hahn (Kluwer Academic, Boston, 2002).
- [11] A. Kuhn, R. Eger, J. Nuss, and B. V. Lotsch, *Z. Anorg. Allg. Chem.* **640**, 689 (2014).
- [12] P. Hohenberg and W. Kohn, *Phys. Rev.* **136**, B864 (1964).
- [13] W. Kohn and L. J. Sham, *Phys. Rev.* **140**, A1133 (1965).
- [14] P. Giannozzi, S. de Gironcoli, P. Pavone, and S. Baroni, *Phys. Rev. B* **43**, 7231 (1991).
- [15] X. Gonze, *Phys. Rev. B* **55**, 10337 (1997).
- [16] X. Gonze and C. Lee, *Phys. Rev. B* **55**, 10355 (1997).
- [17] S. Baroni, S. De Gironcoli, A. Dal Corso, and P. Giannozzi, *Rev. Mod. Phys.* **73**, 515 (2001).
- [18] P. Giannozzi and S. Baroni, in *Handbook of Materials Modeling*, edited by S. Yip (Springer, Berlin, 2005), pp. 195–214.
- [19] X. Gonze, F. Jollet, F. A. Araujo, D. Adams, B. Amadon, T. Applencourt, C. Audouze, J.-M. Beuken, J. Bieder, A. Bokhanchuk, E. Bousquet, F. Bruneval, D. Caliste, M. Côté, F. Dahm, F. D. Pieve, M. Delaveau, M. D. Gennaro, B. Dorado, C. Espejo *et al.*, *Comput. Phys. Commun.* **205**, 106 (2016), available at <http://www.abinit.org>
- [20] P. Giannozzi, O. Andreussi, T. Brumme, O. Bunau, M. Buongiorno Nardelli, M. Calandra, R. Car, C. Cavazzoni, D. Ceresoli, M. Cococcioni, N. Colonna, I. Carnimeo, A. Dal Corso, S. de Gironcoli, P. Delugas, R. A. DiStasio, A. Ferretti, A. Floris, G. Fratesi, G. Fugallo *et al.*, *J. Phys.: Condens. Matter* **29**, 465901 (2017), available at <http://www.quantum-espresso.org>
- [21] P. E. Blöchl, *Phys. Rev. B* **50**, 17953 (1994).
- [22] N. A. W. Holzwarth, A. R. Tackett, and G. E. Matthews, *Comput. Phys. Commun.* **135**, 329 (2001), available at <http://pwpaw.wfu.edu>
- [23] N. A. W. Holzwarth, *Comput. Phys. Commun.* **243**, 25 (2019).
- [24] K. Momma and F. Izumi, *Appl. Crystallogr.* **44**, 1272 (2011), code available at <http://jp-minerals.org/vesta/en/>
- [25] A. Kokalj, *Comput. Mater. Sci.* **28**, 155 (2003), code available at <http://www.xcrysden.org>
- [26] H. T. Stokes and D. M. Hatch, *J. Appl. Crystallogr.* **38**, 237 (2008), available at <http://iso.byu.edu/iso/isotropy.php>
- [27] MERCURY 3.5.1 (2014), developed and distributed by the Cambridge Crystallographic Data Centre, <http://www.ccdc.cam.ac.uk/mercury/>
- [28] M. I. Aroyo, J. M. Perez-Mato, D. Orobengoa, E. Tasci, G. De La Flor, and A. Kirov, *Bulg. Chem. Commun.* **42**, 183 (2011), available at <http://www.cryst.ehu.es/>
- [29] J. P. Perdew and Y. Wang, *Phys. Rev. B* **45**, 13244 (1992).
- [30] Y. A. Du and N. A. W. Holzwarth, *Phys. Rev. B* **76**, 174302 (2007).
- [31] G. Petretto, S. Dwaraknath, H. P.C. Miranda, D. Winston, M. Giantomassi, M. J. van Setten, X. Gonze, K. A. Persson, G. Hautier, and G.-M. Rignanese, *Sci. Data* **5**, 180065 (2018).
- [32] L. He, F. Liu, G. Hautier, M. J. T. Oliveira, M. A. L. Marques, F. D. Vila, J. J. Rehr, G.-M. Rignanese, and A. Zhou, *Phys. Rev. B* **89**, 064305 (2014).
- [33] J. P. Perdew, A. Ruzsinszky, G. I. Csonka, O. A. Vydrov, G. E. Scuseria, L. A. Constantin, X. Zhou, and K. Burke, *Phys. Rev. Lett.* **100**, 136406 (2008).
- [34] M. Born and K. Huang, *Dynamical Theory of Crystal Lattices* (Oxford University Press, Oxford, 1954).
- [35] A. A. Maradudin, E. W. Montroll, G. H. Weiss, and I. P. Ipatova, *Theory of Lattice Dynamics in the Harmonic Approximation*, 2nd ed., Solid State Physics: Supplement (Academic, New York, 1971), Vol. 3.
- [36] H. J. Monkhorst and J. D. Pack, *Phys. Rev. B* **13**, 5188 (1976).
- [37] J. Howard, Z. D. Hood, and N. A. W. Holzwarth, *Phys. Rev. Mater.* **1**, 075406 (2017).
- [38] Y. Li, W. C. Kerr, and N. A. W. Holzwarth, *J. Phys.: Condens. Matter* **32**, 055402 (2019).
- [39] X. Gonze, B. Amadon, G. Antonius, F. Arnardi, L. Baguet, J.-M. Beuken, J. Bieder, F. Bottin, J. Bouchet, E. Bousquet, N. Brouwer, F. Bruneval, G. Brunin, T. Cavignac, J.-B. Charraud, W. Chen, M. Côté, S. Cottenier, J. Denier, G. Geneste *et al.*, *Comput. Phys. Commun.* **248**, 107042 (2019).
- [40] Y. A. Du and N. A. W. Holzwarth, *ECS Trans.* **25**, 27 (2010).
- [41] P. Umari, A. Pasquarello, and A. Dal Corso, *Phys. Rev. B* **63**, 094305 (2001).
- [42] M. Veithen, X. Gonze, and P. Ghosez, *Phys. Rev. B* **71**, 125107 (2005).
- [43] S. A. Prosandeev, U. Waghmare, I. Levin, and J. Maslar, *Phys. Rev. B* **71**, 214307 (2005).
- [44] H. Hamaguchi, in *Advances in Infrared and Raman Spectroscopy*, edited by R. J. H. Clark and R. E. Hester (Wiley, New York, 1985), Vol. 12, pp. 273–310.
- [45] H. Jónsson, G. Mills, and K. W. Jacobsen, in *Classical and Quantum Dynamics in Condensed Phase Simulations*, edited by B. J. Berne, G. Cicciotti, and D. F. Coker (World Scientific, Singapore, 1998), pp. 385–404.
- [46] G. Henkelman, B. P. Uberuaga, and H. Jónsson, *J. Chem. Phys.* **113**, 9901 (2000).
- [47] G. Henkelman and H. Jónsson, *J. Chem. Phys.* **113**, 9978 (2000).
- [48] L. Verlet, *Phys. Rev.* **159**, 98 (1967).
- [49] X. He, Y. Zhu, A. Epstein, and Y. Mo, *npj Comput. Mater.* **4**, 18 (2018).
- [50] G. E. Murch, *Solid State Ionics* **7**, 177 (1982).
- [51] J. D. Howard and N. Holzwarth, *Solid State Ionics* **325**, 80 (2018).
- [52] K. Campaan and Y. Haven, *Trans. Faraday Soc.* **54**, 1498 (1958).

- [53] Y. Haven and B. Verkerk, *Phys. Chem. Glasses* **6**, 38 (1965).
- [54] D. Hicks, M. J. Mehl, E. Gossett, C. Toher, O. Levy, R. M. Hanson, G. Hart, and S. Curtarolo, *Comput. Mater. Sci.* **161**, S1 (2019).
- [55] M. J. Mehl, D. Hicks, C. Toher, O. Levy, R. M. Hanson, G. Hart, and S. Curtarolo, *Comput. Mater. Sci.* **136**, S1 (2017).
- [56] Y. Hinuma, G. Pizzi, Y. Kumagai, F. Oba, and I. Tanaka, *Comput. Mater. Sci.* **128**, 140 (2017).
- [57] D. R. Hamann, *Phys. Rev. B* **88**, 085117 (2013).
- [58] M. van Setten, M. Giantomassi, E. Bousquet, M. Verstraete, D. Hamann, X. Gonze, and G.-M. Rignanese, *Comput. Phys. Commun.* **226**, 39 (2018), data sets available at <http://www.pseudo-dojo.org/>
- [59] A. Brown and S. Rundqvist, *Acta Crystallogr.* **19**, 684 (1965).
- [60] S. J. Rettig and J. Trotter, *Acta Crystallogr., Sect. C: Cryst. Struct. Commun.* **43**, 2260 (1987).
- [61] K. Homma, M. Yonemura, T. Kobayashi, M. Nagao, M. Hirayama, and R. Kanno, *Solid State Ionics* **182**, 53 (2011).
- [62] P. C. Minshall and G. M. Sheldrick, *Acta Crystallogr. B* **34**, 1326 (1978).
- [63] M. Jansen and U. Henseler, *J. Solid State Chem.* **99**, 110 (1992).
- [64] A. Vos, R. Olthof, F. van Bolhuis, and R. Botterweg, *Acta Crystallogr.* **19**, 864 (1965).
- [65] M. R. Sørensen and A. F. Voter, *J. Chem. Phys.* **112**, 9599 (2000).
- [66] Y. Mo, S. P. Ong, and G. Ceder, *Chem. Mater.* **24**, 15 (2012).